



Extracting charge carrier mobility in organic solar cells through space-charge-limited current measurements

Dongcheng Jiang^a, Jiangkai Sun^a, Ruijie Ma^b, Vox Kalai Wong^c, Jianyu Yuan^d, Kun Gao^a, Feng Chen^a, Shu Kong So^c, Xiaotao Hao^a, Gang Li^b, Hang Yin^{a,*}

^a School of Physics, State Key Laboratory of Crystal Materials, Shandong University, Jinan 250100, PR China

^b Department of Electrical and Electronic Engineering, Research Institute for Smart Energy (RISE), Photonic Research Institute (PRI), The Hong Kong Polytechnic University, Kowloon, Hong Kong SAR 999077, PR China

^c Department of Physics and Institute of Advanced Materials, Hong Kong Baptist University, Kowloon Tong, Hong Kong SAR 999077, PR China

^d Institute of Functional Nano & Soft Materials (FUNSOM), Soochow University, Suzhou 215123, PR China



ARTICLE INFO

Keywords:

Space-charge-limited current measurement
Charge carrier transport
Thick-film all-polymer organic solar cells

ABSTRACT

Mobility is a critical parameter influencing the overall performance of organic solar cells (OSCs). Herein, we innovatively elucidated the intricate interrelation between the photovoltaic molecular structures and the methodologies employed for the extraction of charge carrier mobility in OSCs. We proposed a simple yet effective principle to accurately extract charge carrier mobility values using the standard space-charge-limited current (SCLC) measurement, while critically assessing theoretical and experimental deficiencies through the drift-diffusion analysis. It was found that field-dependent charge transport is necessitated to describe the prominent long-range intrachain hopping carrier behavior in polymers, while short-range intermolecular hopping results in trap-involved charge transport within small molecular acceptors. Based on the above understanding, a synergistic inter/intra-molecular hopping strategy was proposed to fabricate thick-film all-polymer OSCs, and an unprecedented power conversion efficiency (PCE) of 16.61 % was achieved in the 300 nm PM6:PY-IT OSC. This work not only presents a precise and straightforward approach for measuring mobility values, but also provides a significant reference about charge carrier transport to make optimal decisions regarding photovoltaic material design and device fabrication process of high-performance OSCs.

1. Introduction

Charge carrier transport is a crucial process of the overall performance of organic solar cells (OSCs) [1–3]. Mobility, defined as the average drift velocity of charge carriers in response to an applied voltage, represents a crucial parameter to evaluate the charge carrier behaviors as it characterizes how quickly charge carriers can move through OSCs when pulled by an external electric field. In the early years, it was a measure of the properties exhibited by Bloch electrons (holes) within the band theory, which was initially used to describe inorganic semiconductors and was strongly dependent on the Fermi surface and effective mass [4,5]. With the rise of organic semiconductors, people proposed that the localization of eigenstates and the presence of strong electron-phonon coupling give rise to distinct charge carrier transport modes, specifically the phonon-assisted and transient localization modes [6–8]. The OSC system is a more complex case, as the

intricate electron-hole bi-continuous networks formed by the donor-acceptor blending in bulk heterojunction (BHJ) films [9,10]. In OSCs, mobility is highly correlated with the photovoltaic parameters involving the short-circuit current density (J_{sc}), open-circuit voltage (V_{oc}), and fill factor (FF). Various phenomenological models have been proposed to investigate the transport-related photovoltaic conversion processes [11,12]. Especially, widely-used Onsager-Braun model and Langevin-type bimolecular recombination model clearly state the effects of charge carrier behaviors in the separation of charge transfer (CT) states and non-radiative energy losses [13–15]. Therefore, accurately extracting mobility values in OSCs is extremely significant in both the fundamental research and device optimization.

Regrettably, existing methodologies appear to run counter to the precise and expedient criteria necessary for extracting mobility values in organic solar cells (OSCs). To date, the space-charge-limited current (SCLC) technique has emerged as the predominant approach for

* Corresponding author.

E-mail address: hyin@sdu.edu.cn (H. Yin).

simulating charge carrier behaviors, owing to its evident accessibility and compatibility with conventional active layer thicknesses of OSCs [16–18]. Typically, the measured current density (J), subject to the space-charge limitation, exhibits a responsive relationship with the applied voltage (V) and can be modeled by using the Mott-Gurney (MG) equation expressed as $J = 9/8\epsilon\mu V^2/L^3$, where ϵ is the permittivity of the organic semiconductors. Nonetheless, the uncritical derivation of mobility from a seemingly plausible $J \propto V^2$ regime may lead to substantial inaccuracies due to overlooking the hypotheses related to traps in SCLC derivation. The existence of charge carrier traps and energetic distribution are the cornerstones of SCLC model differentiation [19]. The Mark-Helfrich (MH) model, which is characterized by $J \propto V^{l+1}$ (where $l > 1$), is suitable for describing carrier behavior associated with exponential tail states. On the other hand, the Rose-Lampert (RL) model, characterized by $J \propto V^2$ similar to the MG equation, is fitting for describing carrier behavior linked to mid-gap deep traps [20–22]. Different SCLC models may exhibit comparable current density-voltage dependencies potentially leading to misleading model selection, which underscore the need to possess dependable criteria for model selection. Additionally, another misconception regarding SCLC measurements pertains to the failure to evaluate the fundamental presumptions inherent in the SCLC derivation. This encompasses the oversight of diffusion current, unipolar charge carrier transport, and the existence of ohmic contacts at both electrode interfaces [23,24]. The aforementioned issues in mobility extraction can give rise to notable discrepancies in accuracy. Any ambiguous mobility extraction not only impedes the fundamental understanding of transport-related processes complicating the establishment of effective numerical analysis model, but also misguides the structure-property relationships introducing deviations in the device optimization process.

In this work, we innovatively elucidated the intricate interrelation between the photovoltaic molecular structures and the methodologies employed for the extraction of charge carrier mobility in OSCs. First, we examined the crucial role of the slope function $g(V)$ in mobility extraction in typical BHJ films, and analyzed the impact of ideal assumptions on the mobility extraction, including injection/extraction barriers and the contribution of diffusion current. Based on the above assessment, we proposed a simple yet effective approach for accurate mobility extraction employing the standard SCLC measurement. We establish a connection between the methodologies for the mobility extraction model and the molecular structure of photovoltaic materials. Building upon this understanding, we adopted the solid additive approach to establish the synergistic inter/intra-molecular hopping mode for electron transport, and fabricated high-performance thick-film all-polymer solar cells (APSCs) based on PM6:PY-IT achieving an unprecedented power conversion efficiency (PCE) of 16.61 % in the 300 nm device. This work not only presents a precise and straightforward approach for measuring mobility values, but also provides a significant reference about charge carrier transport to make optimal decisions regarding photovoltaic material design and device fabrication process of high-performance OSCs.

2. Results and discussion

2.1. Critical assessment of SCLC measurement

Fig. 1 lists the chemical structures and energy levels of selected photovoltaic materials in this work. Single-carrier devices were fabricated to evaluate the charge transport behaviors with the structures of ITO/PEDOT:PSS/Active Layer/Spiro-TPD/Au for holes and ITO/Al/Active Layer/PDINN/Ag for electrons (Fig. S1). The SCLC model was adopted as the simulation method and has been well documented in the Supplementary Information. Fig. 2a summarizes the extracted hole and electron mobilities in typical polymer:fullerene, polymer:non-fullerene acceptor (NFA), all-polymer and single-component active layers with the SCLC measurement. We first compared four widely-used Mott-

Gurney, Rose-Lampert, Mark-Helfrich and Poole-Frenkel (PF) models. It is evident that indiscriminate analytical model selection leads to at least one order (even up to three orders) of magnitude difference in mobility values across various BHJ and single-component cases. In the case of PTB7-Th:IEICO-4F blend, the electron mobility (μ_e) values are 1.5×10^{-3} and $6.5 \times 10^{-7} \text{ cm}^2\text{V}^{-1}\text{s}^{-1}$ fitting by the RL and PF models, respectively. This discrepancy can be attributed to the distinct applicable conditions for differentiated SCLC models, emphasizing the necessity of effective model selection criteria. These models are differentiated based on the energetic distribution of traps involved. The utilization of the trap-free (MG) model is appropriate either in scenarios where traps are not taken into consideration or when they are filled. The RL model arises when discrete traps are present, while the MH model is derived when exponential shallow traps are considered. In the last two models, charge transport is influenced by the presence of traps, which can be described as "trap-filling" charge transport modes. Building upon the MG model, the PF model is formulated, incorporating with the field-dependent Poole-Frenkel effect [25]. Therefore, selecting the appropriate model is the prerequisite to accurately estimate device mobility values. Fig. 2b provides an overview of the main challenges of the SCLC analysis in both the theoretical assumption and experimental limitation aspects. The derivation of SCLC models necessitates several ideal theoretical assumptions as below: i) the neglect of diffusion current, ii) the presence of two ohmic contacts sandwiching the active layer, and iii) the exclusive contribution of the injected charge for the variation of the internal electric field. However, it is difficult to satisfy the above ideal assumptions perfectly in reality, which requires careful evaluation of the influence of relevant parameters including diffusion current contribution, injection/extraction barriers, and the built-in electric field on mobility extraction. Furthermore, electron current leakage and the resulting interface recombination are the experimental limitations to be considered in hole-only devices, especially when using MoO_3 as the electron-blocking interlayer (EBL) due to its moderate electron affinity of MoO_3 [26]. Conversely, Spiro-TPD with low electron affinity is suitable for the EBL, which can effectively prevent electron current leakage in hole-only devices [27]. It is important to note the modification of the cathode work function by widely-used interlayers, such as PDI derivatives, may also affect the contact barrier and the built-in electric field in electron-only devices [28]. Even if the contacts are made from the same material, the built-in electric field should be considered. In summary, it is suggested to carefully evaluate the impact of the diffusion current and built-in electric field in electron-only devices. Meanwhile, the non-ohmic contact, built-in field and electron current leakage in hole-only devices can potentially affect the accuracy of extracted mobility values. Fig. 2c provides a systematic description of the impact of diffusion current, non-ohmic contacts and electron current leakage on carrier transport behavior. As illustrated in Fig. S2, the threshold for the validity of the SCLC models can be analytically calculated to exceed 1 V at the room temperature, which is in a critical voltage where diffusion contributions for both MG and MH models can indeed be ignored. Charge accumulation at the interface formed by the non-ohmic contacts affects the SCL current in the device, leading to significant mobility deviations. In general, injection/extraction barriers below 0.4 eV can be considered as near-ohmic contacts, which still facilitate reasonable mobility extraction, provided that the device is not too thin (> 100 nm) [29,30]. Considering the deviation of simulated mobility and economic considerations, it is advisable to maintain the device thickness at approximate 200 nm to extract mobility values by using SCLC techniques. To ensure that charge carrier mobility is extracted accurately by SCLC measurement, we recommend the following guidelines. First, it is important to analyze the slope of current density-voltage (J - V) curves: $g(V) = d \ln J/d \ln V$, which represents the current density-voltage dependence. It is feasible to distinguish differentiated SCLC models by analytical checkout of current density-voltage dependence. When $g(V)$ remains a constant value (2 ± 0.2) in the intermediate voltage region, the MG model should be chosen in such cases. Although both the MG and

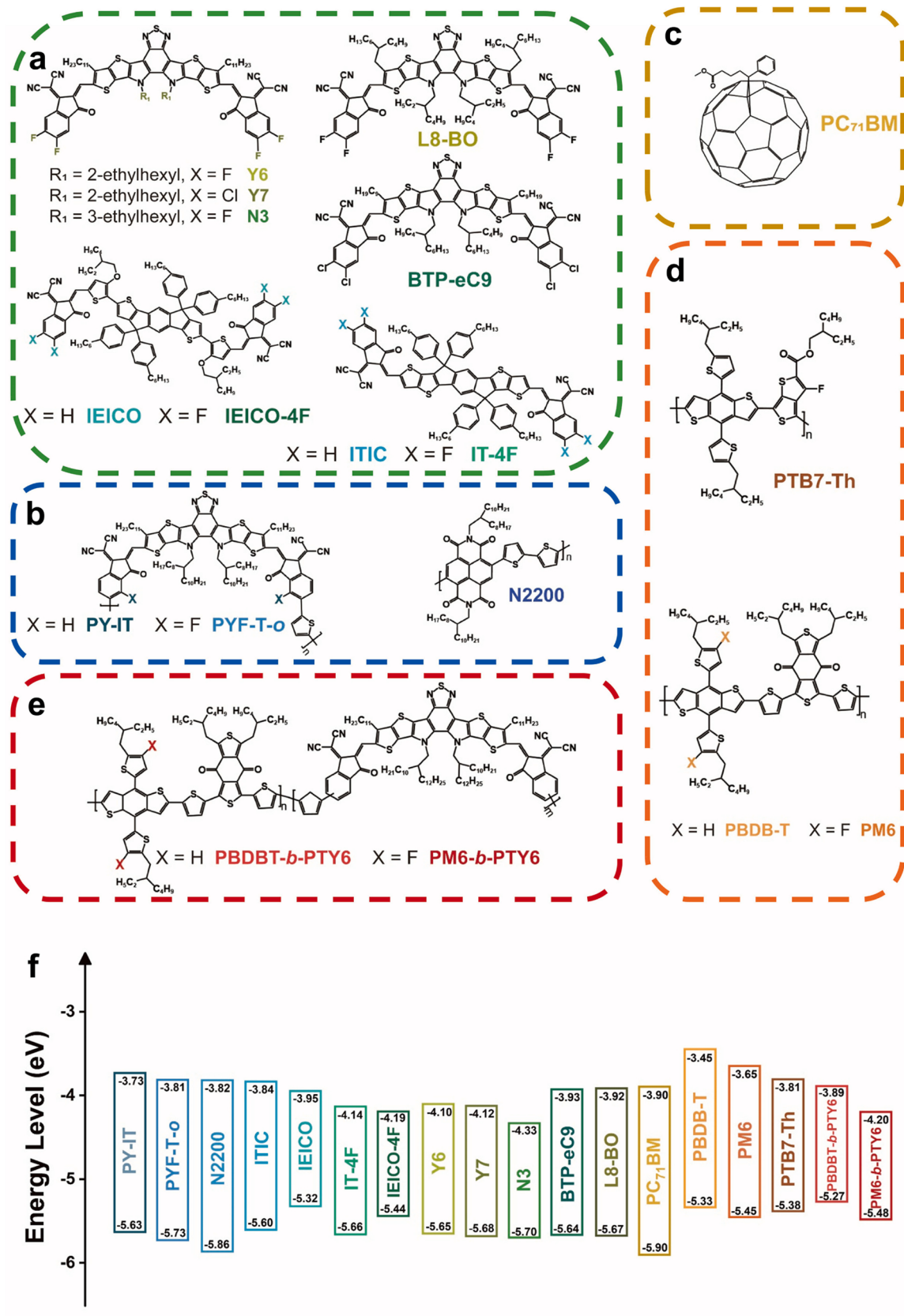


Fig. 1. Chemical structures and energy levels. (a) Chemical structure of small molecular acceptors, (b) polymer acceptors, (c) fullerene acceptor, (d) polymer donors and (e) single-component materials. (f) Energy level diagrams of photovoltaic materials.

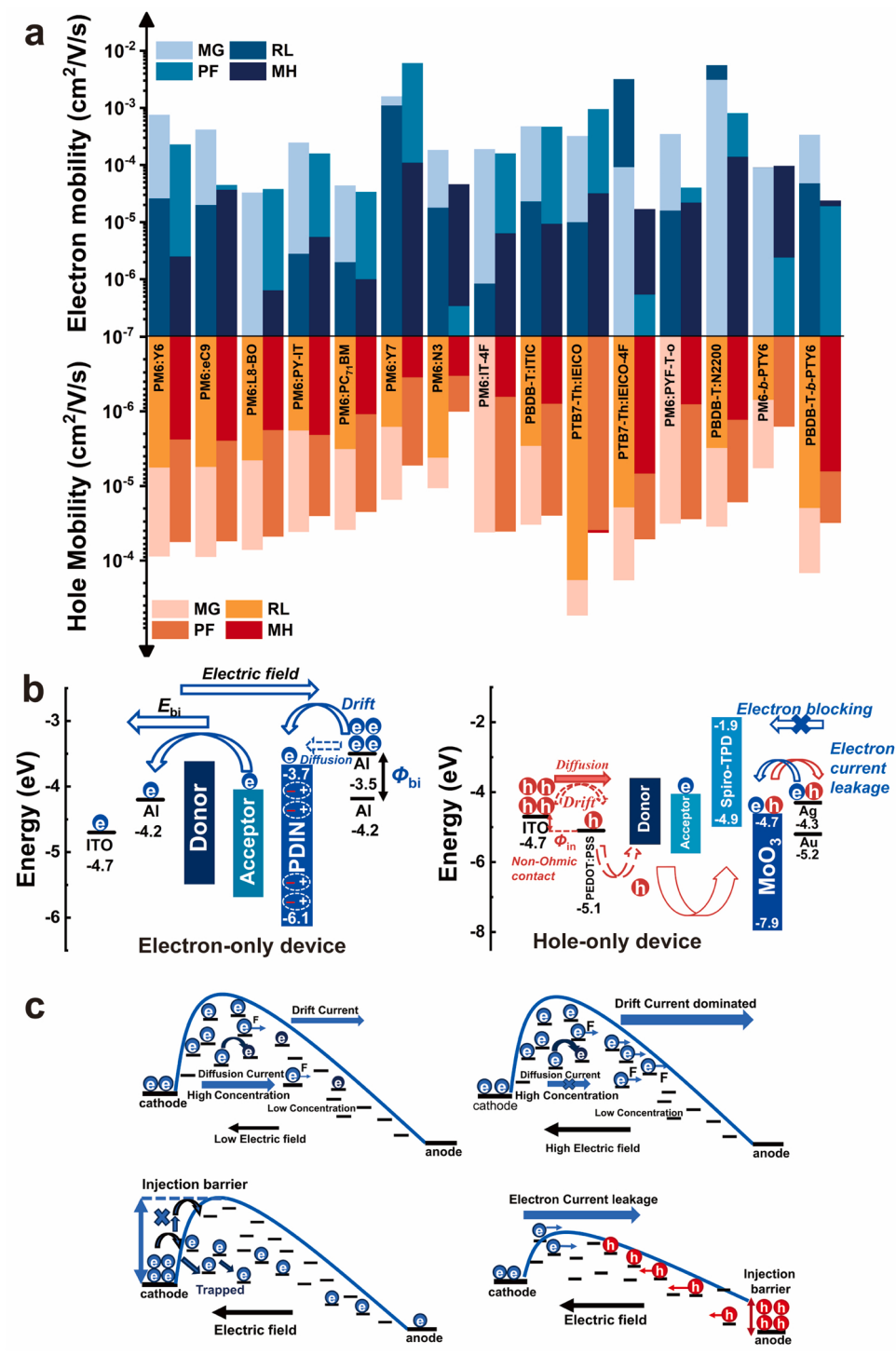


Fig. 2. Critical assessment of mobility extraction in SCLC measurement. (a) Comparison of mobility values extracted by differentiated SCLC models. (b) Overview of the main challenges in SCLC analysis in both theoretical assumption and experimental limitation aspects. For electron-only device: Diffusion current contribution, built-in field; For hole-only device: Diffusion current contribution, non-ohmic contact, electron current leakage and built-in field. (c) Illustration of carrier transport in single-carrier devices with non-ideal characteristics including diffusion current contribution, non-ohmic contact, and electron current leakage.

RL models exhibit the same current-voltage dependence, the RL model incorporates the presence of deep discrete traps. Charge carrier injection leads to the filling of these traps resulting in a distinct slope transition in the high voltage range. This transition serves as a sign of distinguishing the MG and RL models [31]. Similarly, the MH model is suitable for cases where $g(V)$ is a constant above 2 in the intermediate voltage region. The PF model is appropriate when $g(V)$ has a unique phenomenon

of continuous increase in the intermediate voltage region. Combining the J - V curves with $g(V)$ curves is a powerful analytical approach for analyzing SCLC data. Secondly, while ensuring the selection of the appropriate model, we need to further consider two factors: 1) Expanding the voltage measurement range becomes essential. This not only guarantees the neglect of diffusion current but also mitigates uncertainties of the slope transition; 2) Selecting suitable electrodes and

interlayers is imperative to minimize contact barriers and clarify the built-in electric field. In summary, the accurate extraction of charge carrier mobilities relies on the tandem effects of reasonable single-carrier device structures, correct model selection based on $g(V)$, and an extended voltage measurement range (≥ 4 V).

2.2. Mobility extraction guidelines

Fig. 3 illustrates the steps to extract mobility values with typical PM6-based BHJ films with acceptors of Y6, BTP-eC9, L8-BO, PY-IT, and PC₇₁BM. As shown in Fig. 3a and b, the experimentally measured

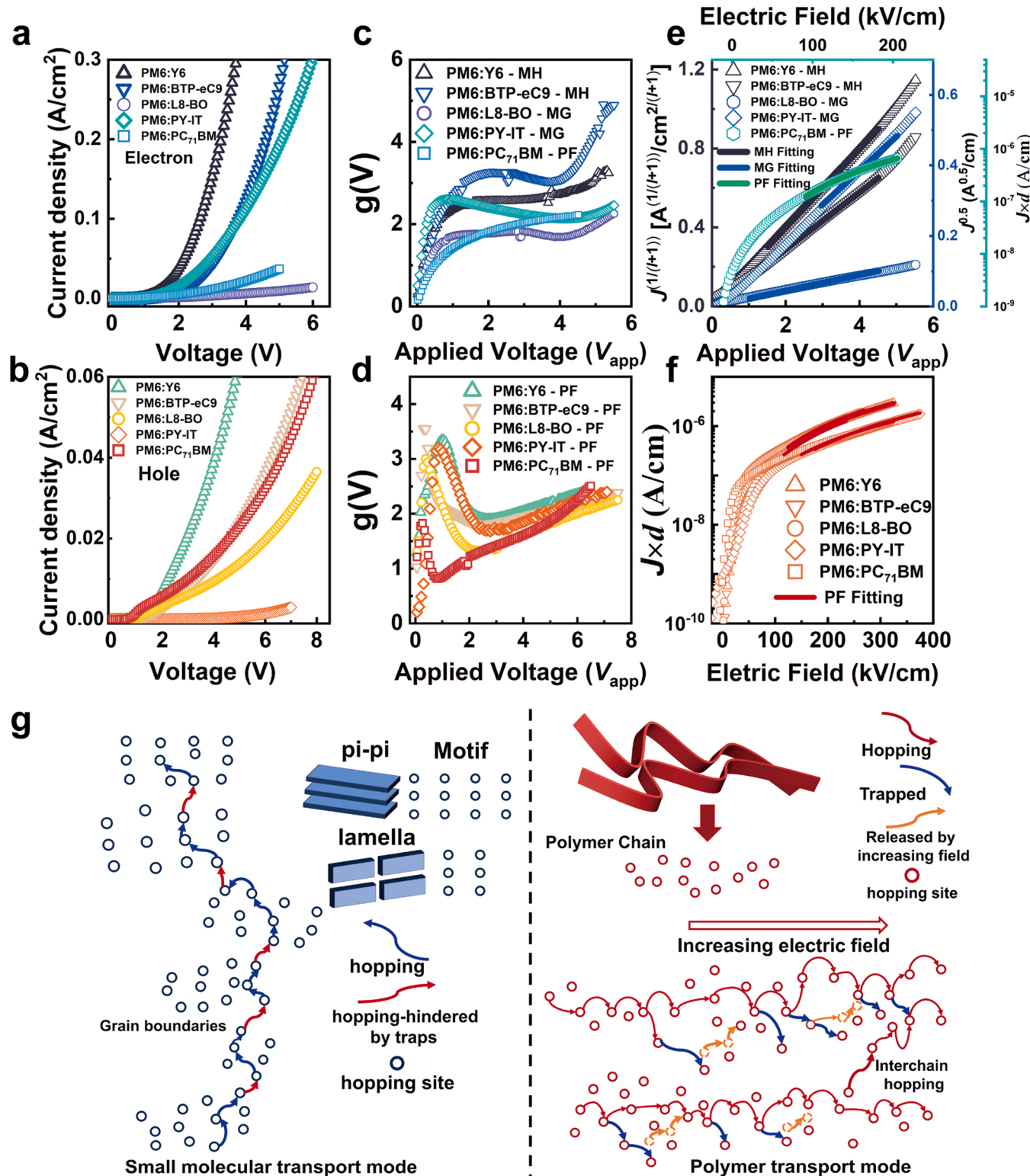


Fig. 3. Mobility extraction guidelines. Current density versus voltage characteristics of electron-only device (a) and hole-only device (b) based on different acceptors blend films. Summary of the slope of J - V curves for electrons (c) and holes (d). Electron (e) and hole (f) J - V curves were analyzed by differentiated SCLC models depending on the model selection criteria. (g) Schematic representation of charge carrier transport modes in small molecules (blue) and polymers (red).

electron and hole J-V curves are displayed for selected BHJ films. Fig. 3c shows the g(V) curves of the electron-only device across five BHJs. The g(V) curve of the PM6:PC₇₁BM film presents a consistent upward trend, indicating the suitability of employing the PF model to describe the transport behavior. μ_e , extracted through the PF model, is determined as $4.3 \times 10^{-5} \text{ cm}^2 \text{V}^{-1} \text{s}^{-1}$. For other BHJs, the g(V) curves exhibit plateaus in the intermediate voltage region. Here, the average value of g(V) in the platform interval is employed to represent the characteristic value. For the PM6:L8-BO and PM6:PY-IT cases, with eigenvalues around 2 ($g = 1.8, 2.1$), these two BHJs fall within the applicable range of the MG model, which means that electrons can flow freely in such small molecular acceptors without being affected by traps. μ_e are $3.4 \times 10^{-5} \text{ cm}^2 \text{V}^{-1} \text{s}^{-1}$ for L8-BO and $2.5 \times 10^{-4} \text{ cm}^2 \text{V}^{-1} \text{s}^{-1}$ for PY-IT, as determined using the MG model. Furthermore, PM6:Y6 and PM6:BTP-eC9 BHJ films display eigenvalues greater than 2 ($g = 2.8, 3.1$), necessitating the utilization of the MH model for mobility extraction, which means that the transport of electrons is adversely affected by the exponential tail state. μ_e are $4.1 \times 10^{-5} \text{ cm}^2 \text{V}^{-1} \text{s}^{-1}$ for Y6 and $3.7 \times 10^{-4} \text{ cm}^2 \text{V}^{-1} \text{s}^{-1}$ for BTP-eC9, as determined using the MH model. Consistent with our previous observations, a distinct peak in the slope occurs at low bias (< 1 V), where contacts and deeper traps are more important [32]. The g(V) curve may rapidly rise in the high-voltage range, as the SCLC models are derived with the assumption that mobility is constant, which is usually not true under high electric fields. Conversely, a decreasing slope at high voltage is a sign of series resistance or tortuosity [33]. Therefore, it is meaningful to select the appropriate intermediate voltage region to avoid problems that may make the SCLC model invalid. Fig. 3d shows the g(V) curves of the hole-only device across five BHJs. It can be seen that the g(V) curves of all BHJ films show a rising trend, implying that the field-dependent (PF) model is suitably employed to describe the hole transport in PM6. μ_h are 5.6×10^{-5} (Y6 blends), 6.7×10^{-5} (BTP-eC9 blends), 8.7×10^{-5} (L8-BO blends), 2.7×10^{-5} (PY-IT blends) and $4.4 \times 10^{-5} \text{ cm}^2 \text{V}^{-1} \text{s}^{-1}$ (PC₇₁BM blends), as determined using the PF model. Similarly, the g(V) curves of the hole-only devices across PBDB-T-based blends, PTB7-Th-based blends and single component devices consistently rise, affirming the applicability of the PF model to describe hole transport. Furthermore, the PF model also characterizes electron transport in the polymer acceptor N2200. The coexistence of high-molecular-weight polymers with the PF model suggests that the charge transport properties in these polymers precisely match the field-dependent form described by the PF model. This alignment is rooted

in the intrinsic properties of high-molecular-weight polymers, which are thoroughly discussed in Section 2.4. Additionally, mobilities of the pristine acceptors and donors were estimated as listed in Table S1. The reasonable variations in mobility between pristine and BHJ films may be attributed to differences in crystallinity. As depicted in Fig. 3e and f, in accordance with the chosen SCLC model, numerical analysis effectively validates the data's compatibility with the fitting curve. The J-V characteristics and the mobility values of electron- and hole-only devices in Fig. 2a are shown in Fig. S3-S12 and Table S2-S3, respectively. Notably, electron and hole transport often fail to satisfy the applicable condition of the RL model across a wide range of devices. This could be attributed to the relatively low density of deep traps in commonly employed photovoltaic materials, which are designed to achieve higher PCEs [34, 35].

2.3. Cross-check mobility

Admittance spectroscopy (AS) and dark-injection (DI) SCLC were performed to verify the accuracy of mobility values extracted from the SCLC measurement. The operation mechanism of AS and DI-SCLC measurements have been well documented elsewhere [36,37]. Fig. 4a to d summarizes the capacitance response as a function of the perturbation frequency of the PM6:Y6 electron-only and hole-only device, respectively. And the transient currents exhibit the electron and hole transit times under different bias voltages as shown in Fig. 4e and f. For the electron-only cell, μ_e values are 5.5×10^{-5} and $2.6 \times 10^{-4} \text{ cm}^2 \text{V}^{-1} \text{s}^{-1}$ from the AS and DI-SCLC measurements, respectively, compared to $4.1 \times 10^{-5} \text{ cm}^2 \text{V}^{-1} \text{s}^{-1}$ extracted by the SCLC measurement. The PF model is employed to extract hole mobility value and the field-dependent parameter β due to different hole transport modes compared to electrons. μ_h achieved by AS and DI-SCLC measurements are 1.6×10^{-5} and $1.3 \times 10^{-5} \text{ cm}^2 \text{V}^{-1} \text{s}^{-1}$, compared to $5.6 \times 10^{-5} \text{ cm}^2 \text{V}^{-1} \text{s}^{-1}$ obtained through the SCLC measurement. The electron and hole mobility values determined from the three measurements are within an order of magnitude. Such slight differences in electron and hole mobilities cross-check the validity of the SCLC measurement guidelines. Furthermore, the relatively higher β_h compared to electrons for each technique indicates a field-dependent transport mode in conjugated polymer systems as shown in Fig. 4h. The mobility values and β for electron and hole are summarized in Table S4.

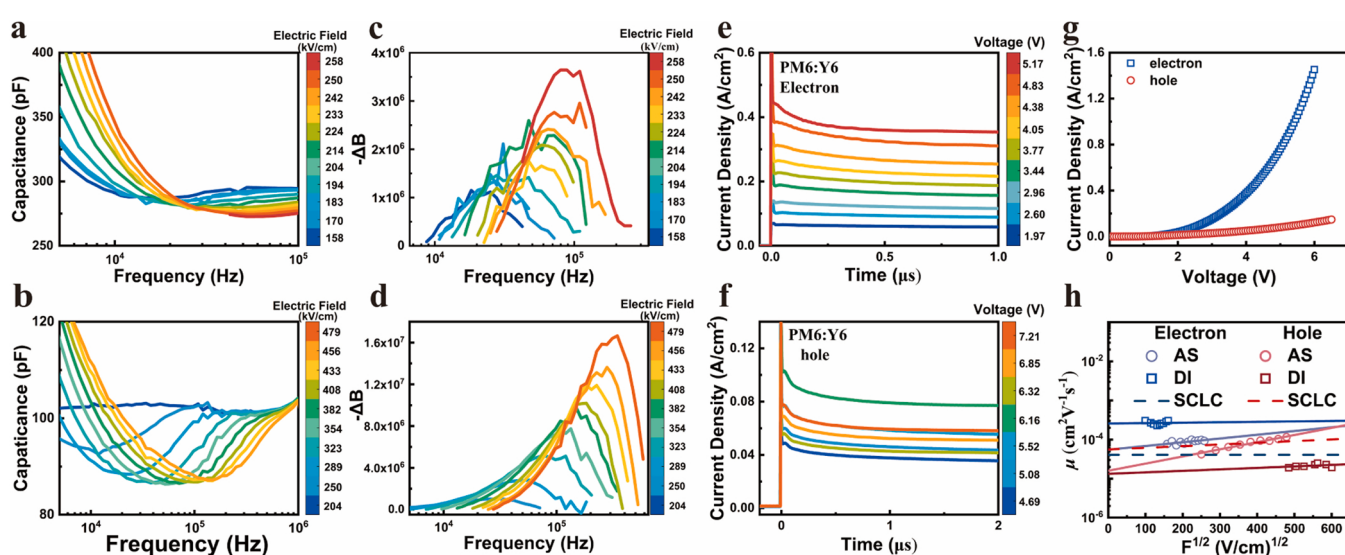


Fig. 4. Cross-validation of the accuracy of mobility extraction for PM6:Y6 BHJ films. The frequency-dependent capacitance characteristics under different bias voltage and $-\Delta B$ as a function of frequency for (a) and (c) electron-only devices and (b) and (d) hole-only devices. A sequence of DI-SCLC signals of electron-only device (e), hole-only device (f). (g) Electron and hole J-V characteristic. (h) The electric field-dependent mobility value is extracted by three techniques.

2.4. Interrelation between the molecular structure and methodology

To clarify how different chemical structures affect carrier transport modes, we investigate the room-temperature Urbach energy (E_U) values of five typical BHJs by photothermal deflection spectroscopy (PDS) and sensitive sub-bandgap external quantum efficiency (s-EQE) techniques. Fig. 5a shows the PDS-derived absorption coefficients versus photon energies of the BHJ films. The E_U can be calculated by the empirical Urbach equation [38], revealing a decreasing trend from 55.7, 25.5, 25.4 to 24.3, and 23.8 meV for PM6:PC₇₁BM, PM6:BTP-eC9, PM6:Y6, PM6:PY-IT, and PM6:L8-BO films, respectively. Additionally, the normalized s-EQE spectra of devices are plotted as a function of the photon energy, as shown in Fig. 5b. The E_U values were calculated from the exponential tail near the band edge of their EQE spectra by $\ln \text{EQE} = c + h\nu/E_U$, where c and $h\nu$ are the constant and photon energy, respectively [39]. All s-EQE spectra display sharp absorption edges that translate into an Urbach energy range from 52.4 to 23.0 meV. The extracted data are highly consistent with those obtained from PDS measurements, and the E_U extracted from both techniques are presented in Table S5. As shown in Fig. 5c, the correlation between the Urbach energy from PDS measurements and electron transport modes can be clearly observed. Smaller Urbach energies usually suggest a flatter charge transport landscape, thus making electron transport in L8-BO and PY-IT suitable for the trap-free transport (MG) mode. Conversely, the trap-filling (MH) mode can be observed in the Y6 and BTP-eC9-based BHJ cases. As the Urbach energy continues rising, the increase of the tail states induces a considerable number of electrons to be bound, and the electric field has a significant effect on the release of trapped electrons [40]. Therefore, the field-dependent PF effect should be considered in the PM6:PC₇₁BM BHJ film. Compared to electron, the hole transport seems less sensitive to traps, as shown in Fig. 5d. The varying sensitivity of carrier transport to traps between small molecules and conjugated polymers can be attributed to distinct carrier transport

modes arising from different molecular structures. Conjugated polymers consist of considerably long and flexible macromolecules, which have numerous conformational degrees and weak interchain interactions [41]. These intrinsic characteristics lead to complex microstructures with varying degrees of order in solid states. In high-molecular-weight semiconducting polymers like PM6, the limited charge transport approach is trapping caused by lattice disorder. This reveals a transport mechanism where mobile charge carriers are temporarily captured in a localized state, akin to multiple capture and release processes, which aligns with the applicable conditions for the PF model [42,43]. Additionally, the arrangement of transport pathways also governs carrier transport modes. Fig. 5g and e provide a summary of the 2D and linecut GIWAXS profiles. For PM6: acceptor blends, PM6 exhibits a dominant face-on orientation with a broad (100) reflection in the in-plane (IP) direction. In this arrangement, effective carrier transport between the two electrodes depends on intrachain-dominated transport modes in conjugated polymers. In such a transport mode, only traps precisely hinder the fastest pathway, the charge transport will be modified, which explains the insensitivity of hole transport to the Urbach energy [44]. Consequently, the field-dependent intrachain-dominated transport mode is commonly observed in high-molecular-weight conjugated polymers, as depicted in Fig. 3g. While, polymer acceptor PY-IT conforms to the trap-free transport mode rather than the field-dependent mode may due to the low polymerization. In comparison to polymers, rigid molecules with stronger intermolecular interactions yield reduced energetic disorder and improved crystallinity. As shown in Fig. 5e, all acceptors reflect pronounced π - π stacking signals in the out-of-plane direction (OOP). This consistent packing orientation indicates that the electron transport in these acceptors, heavily relies on the intermolecular overlapped π -orbitals [45]. During the transport process, carriers must traverse numerous dense molecular packing motifs that serve as “grain boundaries”, hindering carrier transport and leading to sensitivity to traps, as shown in Fig. 3g. Fig. 5f shows parameters derived from the

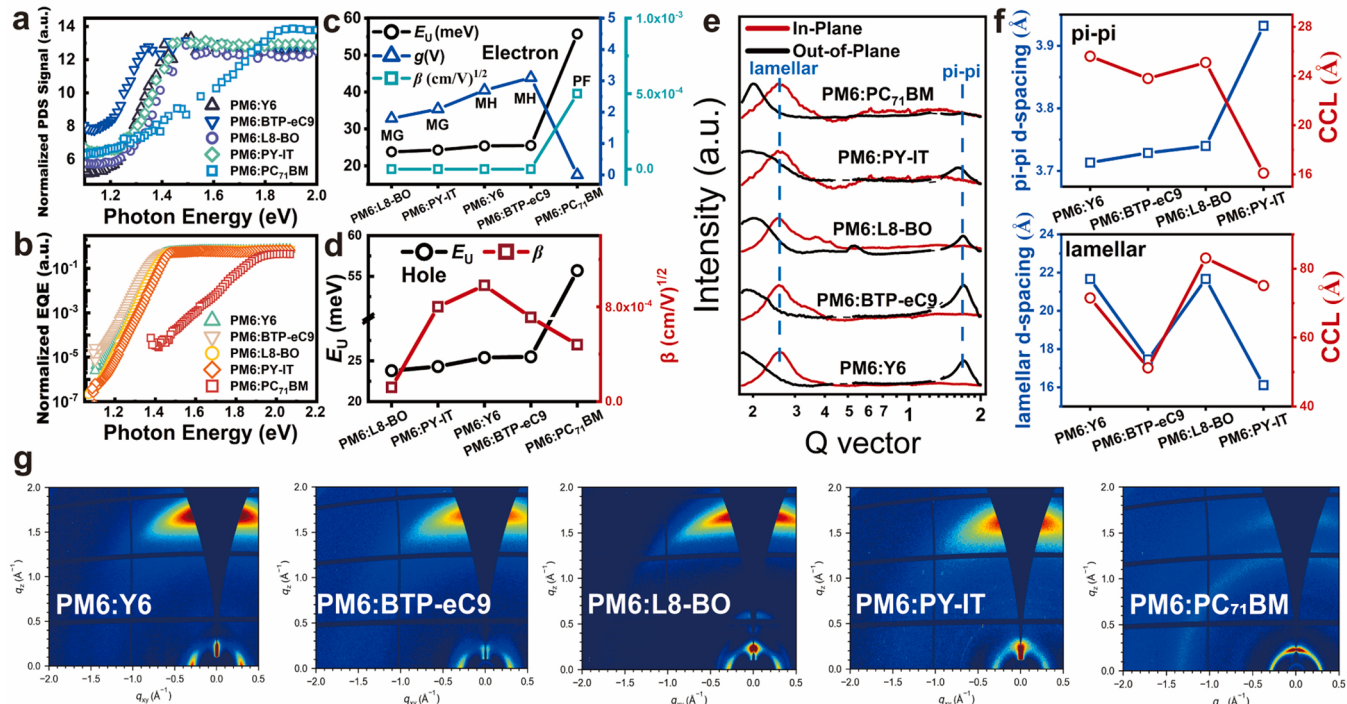


Fig. 5. Correlation of Urbach energy, morphology, and molecular structure. (a) Photothermal deflection spectroscopy (PDS) absorption spectroscopy for determining the Urbach energy (E_U) of five typical BHJs films. (b) Highly sensitive sub-bandgap external quantum efficiency (s-EQE) spectra for E_U extraction. (c) Relationship between E_U and electron transport modes and (d) hole transport modes. (e) Out-of-plane (black) and in-plane (red) linecut profiles of the 2D GIWAXD data. (f) D-spacing (blue symbol) and CCL (red symbol) of pi–pi and lamellae diffraction peaks for blended films with different compositions. (g) 2D GIWAXD patterns of five typical BHJ blends.

$\pi-\pi$ stacking and lamellar peaks of the different BHJ thin films. The crystal coherence lengths (CCLs) for (010) are 25.6 Å (Y6 blends), 23.8 Å (BTP-eC9 blends), 25.1 Å (L8-BO blends) and 16.1 Å (PY-IT blends), as determined using the Scherrer analysis [46]. We further note the differences in the CCLs of the (100) plane signals in the IP direction. The CCLs of the L8-BO and PY-IT blends exhibit larger values (83.1, 75.1 Å), regarding the CCLs of 51.2 Å for BTP-eC9 film and 71.5 Å for Y6 film. Interestingly, this trend correlates to whether carrier transport is hindered by traps in respective devices, pointing to the role of 3D molecular packing in effective carrier transport [47–49]. The difference in the inter-percolated transporting networks for electrons in the blends, affected by molecular stacking of acceptors, is key to distinguish carrier transport models. Thanks to the inter/intra-molecular hopping synergies formed by 3D interpenetrating networks, a balanced short-range intermolecular and long-range intramolecular hopping provides multiple electron transport pathways. This greatly reduces the probability of being hindered by grain boundaries, resulting in trap-free transport in PM6:L8-BO and PM6:PY-IT blend films.

2.5. Device fabrication

Based on the analysis above, we proposed a solid additive approach to improve the device performance of thick-film all-polymer solar cells (APSCs) by regulating the electron transport properties. The loss in FF represents a significant hurdle in the pursuit of high-performance APSCs with thick BHJ films [50,51]. The field-dependent coefficient of mobility, which is related to the trapped carriers released by the electric field, is recognized as a key parameter driving the FF loss [52]. The polymer acceptor PY-IT lacking a field-dependent coefficient, holds a promising candidate to develop outstanding thick-film APSCs through

inter/intrachain synergies transport mode. The Y-series small molecular acceptors (SMAs) including L8-BO, Y6, and BTP-eC9, which exhibit the substantial packing coefficients, are expected to regulate electron transport properties. The introduction of SMA as a solid additive may effectively improve crystallinity through strong interaction with PY-IT, thereby influencing the quality of the 3D interpenetrating networks within PY-IT [53,54]. Consequently, a low dosage (2 wt %) of a series of Y-series SMAs was blended with PM6:PY-IT OSCs to achieve improved thick-film PCEs. The *J-V* curves and external quantum efficiency (EQE) of the PM6:PY-IT-based devices with thin and thick active layers are shown in Fig. 6a and b. The calculated J_{sc} values from EQE spectra are in good agreement with the J_{sc} measured in *J-V* curves. The statistics of APSCs devices are shown in Fig. S13. The photovoltaic parameters of the corresponding OSCs are listed in Table S6. With the increase in thickness, FF dropped from 17.56 to 15.75 % for the control system. For devices with the solid additive treatment, however, FFs decrease gently when the thickness is greater than 200 nm. The comprehensive characterization from morphology, exciton dynamics, charge transport and film forming perspective were employed to gain deeper insights of enhanced performance and "thickness insensitive" of the PM6:PY-IT-based OSCs. The UV-vis absorption spectra of the corresponding thin (100 nm) and thick (300 nm) films are shown in Fig. S14. The blends with SMAs display slightly red-shifted absorption, which suggests a more ordered intermolecular packing of PM6 and PY-IT with the introduction of SMAs in thick films. To gain deeper insights from morphology perspective, atomic force microscopy (AFM) and film-depth-dependent light absorption spectroscopy (FLAS) were performed to determine the effect of SMAs addition on the morphology of thin and thick films. In both thin and thick films, the solid additive-assisted PM6:PY-IT blends exhibit a rough surface with large

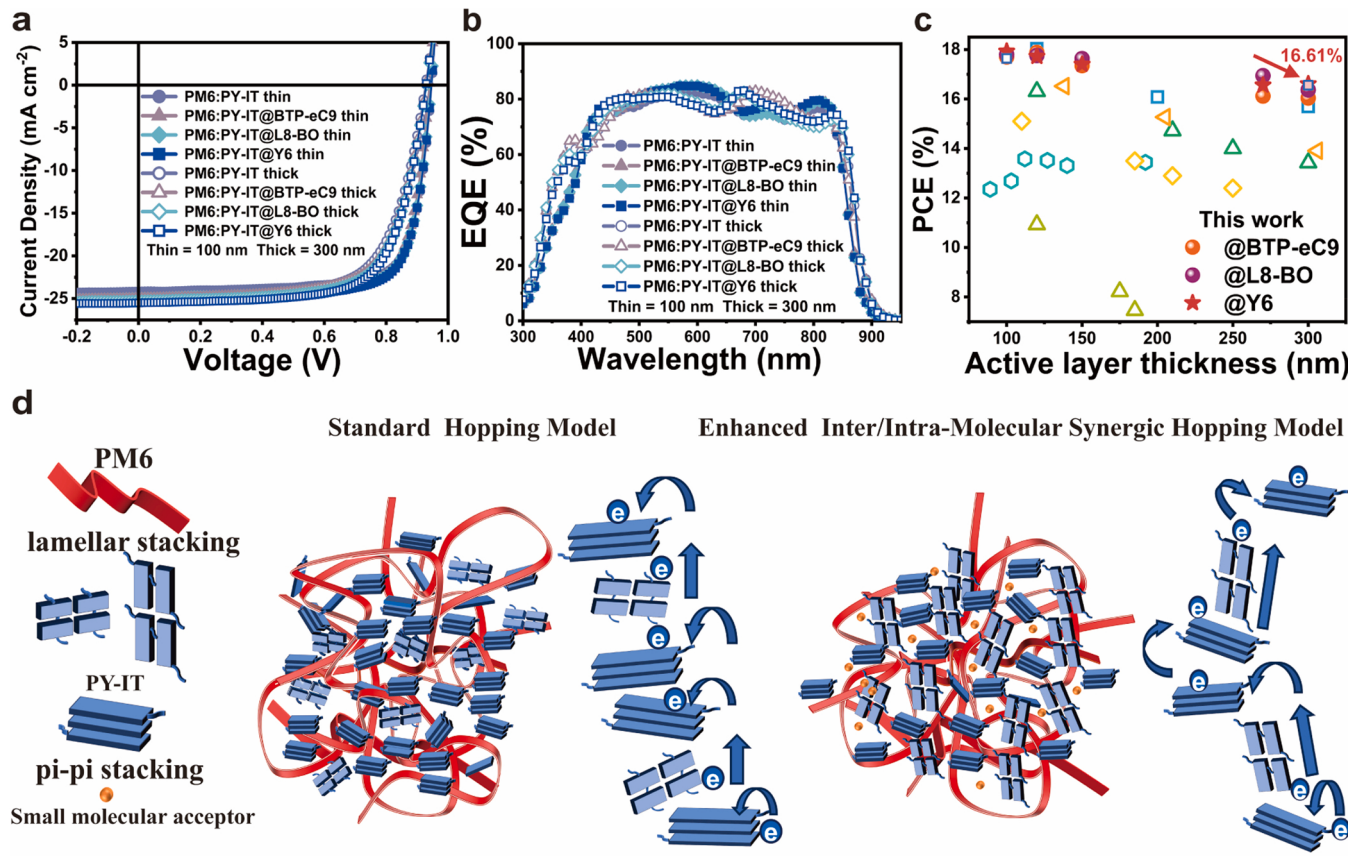


Fig. 6. Photovoltaic properties of thick-film APSCs. (a) *J-V* curves, (b) EQE curves of the PM6:PY-IT-based APSCs with varying active layer thickness. (c) Comparison of our results with previously reported PCEs and thicknesses for APSCs cases. (d) The schematic morphology and transport modes of PM6:PY-IT films (left) and the optimal APSCs with solid additive treatment (right).

root mean square (RMS) values, and bright spots can be seen in the height images, indicative of the fact that SMAs can promote the aggregation of PM6 (Fig. S15). The increased hole mobility observed with solid additive treated further supports that solid additives promote PM6 aggregation (Table S7). While, FLAS measurements reveal that SMAs-assisted thick blend films exhibited more uniform vertical component distributions compared to thick binary blends, which in turn facilitates less bimolecular recombination and promotes charge transport (Fig. S16) [55]. Transient absorption spectroscopy is considered a reliable method for characterizing the charge generation processes in nanoscale films (Fig. S17). Decay dynamic curves probed at 718 nm were subjected to bi-exponential fitting to ascertain the lifetime of exciton dissociation at the D-A interface (τ_1) and exciton diffusion (τ_2), as detailed in Table S8. The maintained τ_1 for the thick films compared to corresponding thin films indicates that solid additive processing leads to a more favorable donor-acceptor interaction in the mixing region matching the results of FLAS measurement [56]. Time-resolved fluorescence lifetime imaging microscopy can be also adopted to visualize the detailed dynamics of the exciton in BHJ films. The mean decay times on the maps are found to be 102.4 ps for the PM6:PY-IT film, while longer lifetimes are observed in blends with SMAs in both thin and thick films, as illustrated in the Fig. S18. The detailed parameters are summarized in Table S9. The increased fluorescence lifetime indicates an extension of the singlet exciton lifetime, which can be ascribed to be the decreased trap state density and more excitons being able to diffuse to the donor-acceptor interface [57]. The in-situ UV-vis absorption measurement was carried out to investigate film evolution kinetics. The locations of the absorption peaks are found almost unchanged with or without SMAs during the film-forming stage (Fig. S19), indicating that a difference working mechanism between SMAs and volatilizable solid additives [58]. Based on above characterizations, the incorporation of SMAs as the solid additive induced PM6 aggregation, and the combination of PY-IT with SMAs exhibited more ordered molecular packing, significantly improving inter/intrachain synergies. Upon introducing SMA, the enhancement in crystallization behavior along the IP direction significantly improves inter/intrachain synergies, while slightly reducing crystallization in the OOP direction [59,60]. Therefore, fluctuations of crystallization within the π - π packing motif lead to an increased presence of grain boundaries that serve as electron traps, aligning the electron transport within the trap-filling model (Fig. S20). Even when electron transport is hindered by traps with the solid additive treatment, the enhanced inter/intrachain synergies within PY-IT still facilitate an effective electron transport pathway as shown in Fig. 6d. The increased electron mobilities suggest that the enhanced inter/intrachain synergies within PY-IT are partially responsible for the higher FFs (Table S10). These synergistic transport modes ultimately lead to the FF pinning effect, significantly slowing the PCE drop in the thick film. As depicted in Fig. 6c, this phenomenon culminates in achieving the record PCE of 16.61 % for a thickness of 300 nm, highlighting the positive impact of this 3D interpenetrating network-induced enhancement (Table S11).

3. Conclusion

In this work, we outlined common pitfalls in mobility extraction employing SCLC measurements and proposed practical recommendations to improve the reliability of mobility extraction. Besides, we elucidated the intricate interrelation between the photovoltaic molecular structures and the methodologies employed for extracting charge carrier mobility in OSCs. We systematically evaluated transport properties in polymer:SMA and polymer:polymer blends and clarified the transport physics of small molecules and polymers. We found that field-dependent charge transport is necessitated to describe the prominent long-range intrachain hopping carrier behavior in polymers, while short-range intermolecular hopping results in trap-involved charge transport within small molecular acceptors. With the synergistic inter-

intra-molecular hopping strategy, the thick-film PM6:PY-IT APSC exhibited a record PCE of 16.61 %. This work proposes a clear method for accurately extracting mobility values and offers insights into the structure-transport property relationship, providing guidelines for optimizing thick-film OSCs.

4. Experimental section/methods

4.1. Materials

Organic photovoltaic materials PBDB-T, PM6, PTB7-Th, ITIC, IT-4F, PY-IT, BTP-eC9, Y6, Y7, L8-BO, N2200 and PDINN used in this work were purchased from Solarmer Materials Inc. N3 and PYF-T-o was purchased from eFlexPV Limited. PEDOT:PSS (Clevios PVP Al 4083) was purchased from Xi'an Polymer Light Technology Corp. Chloroform, methanol, 1,8-Diiodooctane (DIO) and 1-chloronaphthalene were purchased from Sigma Aldrich Inc. All materials were used without further purification.

4.2. Single-carrier device fabrication and characterization

The electron-only devices were fabricated with a conventional configuration of ITO/Al(50 nm)/BHJ/PDINN/Ag. The patterned indium tin oxide (ITO)-coated substrates were sequentially cleaned in an ultrasonic bath by using detergent, deionized water, acetone, absolute ethyl alcohol and isopropyl alcohol for 20 min in each step. These glass substrates were then treated by UV-ozone for 15 min to improve their work function. The 50 nm Al layer deposited onto these cleaned substrates by thermal evaporation is used to block hole carriers. Afterwards, these prepared substrates were transferred into a nitrogen-filled glovebox. The blending solution can be obtained by dissolving an organic donor and acceptor materials through organic solvent such as chloroform (CF). The bulk heterojunction (BHJ) active layer films around 200 nm were fabricated by spin-coating the blend solution on the top of Al and then annealed. After that, a thin layer of PDINN was spin coated on BHJ layer to contribute to the electron transport at 3000 rpm for 30 s. Finally, the top Ag electrodes of 100 nm were deposited on the top of PDINN layer by thermal evaporation to finish the preparation of the whole devices, thus yielding the active area of 0.024 cm² through a shadow mask. The hole-only devices were fabricated with the structure of ITO/PEDOT:PSS/BHJ/Spiro-TPD/Au. The PEDOT:PSS was spin-coated onto these cleaned substrates at 4000 rpm for 50 s and annealed at 150 °C for 15 min in ambient atmosphere. Afterwards, these prepared substrates were transferred into a nitrogen-filled glove box. The BHJ films (~200 nm) were fabricated by spin-coating the blend solution on the top of PEDOT:PSS layer and then annealed. After a 10 nm Spiro-TPD layer deposited by thermal evaporation, an 80 nm Au layer was deposited on the substrate. The current density-voltage (J-V) characteristic curves of all devices were recorded in a low vacuum environment by employing a computer-controlled Keithley 2612B.

4.3. PDS and FTPS measurements

PDS measurements were carried out with a 1 kW Xe arc lamp and a 1/4 m grating monochromator (Oriel) as the tunable light source. The pump beam was modulated at 13 Hz by a mechanical chopper before irradiating on the sample. Perfluorohexane was used as the deflection fluid. A Uniphase HeNe laser as the probe beam was directed parallel to the sample surface. A quadrant cell (United Detector Technology) was used as the position sensor for monitoring the photothermal deflection signal of the probe beam. The output signal of the detector was fed into a lock-in amplifier (Stanford Research, Model SR830) for phase-sensitive measurements. All PDS spectra were normalized to the incident power of the pump beam. The FTPS-EQE measurements were performed by employing a Fourier-transform infrared (FTIR) spectrometer equipped with a halogen lamp light source and an external detector option. The

photocurrent generated from the devices with illumination light modulated by the FTIR instrument was amplified by a low-noise current amplifier. The corresponding photocurrent spectrum were recorded by the FTIR software.

4.4. GIWAXS measurements

GIWAXS measurements were performed upon a film-depth dependent light absorption spectrometer Xeuss 2.0 (Xenocs Inc.) under vacuum conditions. X-rays have a wavelength of 1.54189 Å and sample detector distance calibrated by a silver behenate. Samples were prepared on silicon substrates using identical blend solutions as those used in devices.

4.5. Absorption spectroscopy

UV-vis absorption spectra of the blend films were measured by a UV-Vis-NIR spectrophotometer (Cary 5000, Agilent Technologies, Inc.) under ambient conditions. Samples were fabricated on quartz substrates.

4.6. Atomic force microscope (AFM) image

AFM measurements were performed on a Bioscope Resolve AFM (Bruker) in a tapping mode under ambient conditions.

4.7. Film-depth-dependent light absorption spectroscopy (FLAS)

The film-depth-dependent light absorption spectroscopy was acquired upon a film-depth-dependent light absorption spectrometer (PU100, Puguangweishi Co. Ltd). In-situ soft plasma etching at low pressure (less than 20 Pa) was used to extract the depth-resolved absorption spectrum for the organic active layer. Beer-Lambert's law was utilized to fit the FLAS results, which were subsequently utilized to fit the exciton generation contour upon a modified optical matrix-transfer approach.

4.8. Transient absorption (TA) spectroscopy

The femtosecond TA measurements were performed on an Ultrafast Helios Fire pump-probe system in collaboration with a regenerative amplified laser system from Coherent, Inc. The pump pulses centered at 800 nm were generated by a Ti:Sapphire amplifier (Astrella, Coherent, Inc.) and separated into two parts by a beam splitter. One of the beams was coupled into an optical parametric amplifier (TOPAS, Coherent, Inc.) to generate the pump pulses at 800 nm. The other part was focused onto a sapphire plate and a YAG plate to generate white light as the probe beams with spectra covering 400–1200 nm. The supercontinuum light was split into two beams for balanced detection and ΔA was obtained. The time delay between the pump and probe beams was synchronized and enabled by a digital delay generator. Samples were fabricated on quartz substrates and were encapsulated in a nitrogen glovebox with epoxy resin to minimize air-induced degradation.

4.9. Time-resolved photoluminescence spectroscopy

The TRPL experiments were acquired through a confocal optical microscope (Nanofinder FLEX2, Tokyo Instruments, Inc.) equipped with time-correlated single-photon counting (TCSPC) module (Becker & Hickl, SPC-150). All of the PL spectra were measured using a charge-coupled device (CCD) sensor (DU420A-OE, Andor). The excitation wavelength was fixed at 400 nm.

4.10. In-situ UV-vis absorption measurement

In-situ UV-vis absorption measurements are performed by the DU-

200 dynamic spectrometer in transmission mode with a time resolution of 0.1 s. The spectrometer consists of a light source and a detector. The light source and detector are held above and below the substrate, respectively, and in the same vertical line. The film is coated on a glass substrate and the detector collects transmission spectra from 200 to 1100 nm during the coating process.

Funding

This work was financially supported by the National Natural Science Foundation of China (Grant No. 12204272). H.Y. acknowledges the Shandong Provincial Natural Science Foundation (No. ZR2021QF016/ZR2022YQ04) and the Qilu Young Scholar Program of Shandong University.

Author contributions

H.Y. conceived the ideas and visualization. D.J. performed the charge carrier transport properties, device measurements and data collection, wrote the original draft and visualization. J.S. contributed to the data analysis about the charge carrier transport properties. R.M. fabricated APSCs and conducted the characterization. K.W. performed the PDS measurements. J.Y. provided the study materials. K.G., F.C., S. S., X.H. and G.L. contributed to the research preparation and data analysis. All authors contributed to discussions, manuscript writing, and revisions.

Declaration of Competing Interest

The authors declare that they have no known competing financial interests or personal relationships that could have appeared to influence the work reported in this paper.

Data Availability

Data will be made available on request.

Appendix A. Supporting information

Supplementary data associated with this article can be found in the online version at doi:10.1016/j.mser.2024.100772.

References

- [1] C. Yan, S. Barlow, Z. Wang, H. Yan, A.K.Y. Jen, S.R. Marder, X. Zhan, *Nat. Rev. Mater.* 3 (2018) 18003.
- [2] L. Zhu, M. Zhang, J. Xu, C. Li, J. Yan, G. Zhou, W. Zhong, T. Hao, J. Song, X. Xue, Z. Zhou, R. Zeng, H. Zhu, C.C. Chen, R.C.I. MacKenzie, Y. Zou, J. Nelson, Y. Zhang, Y. Sun, F. Liu, *Nat. Mater.* 21 (2022) 656–663.
- [3] J. Wu, H. Cha, T. Du, Y. Dong, W. Xu, C.-T. Lin, J.R. Durrant, *Adv. Mater.* 34 (2022) 2101833.
- [4] J.B. Costello, S.D. O'Hara, Q. Wu, D.C. Valovcin, L.N. Pfeiffer, K.W. West, M. S. Sherwin, *Nature* 599 (2021) 57–61.
- [5] H. Sato, S.A. Abd. Rahman, Y. Yamada, H. Ishii, H. Yoshida, *Nat. Mater.* 21 (2022) 910–916.
- [6] W. Li, J. Ren, Z. Shuai, *Nat. Commun.* 12 (2021) 4260.
- [7] S. Giannini, A. Carof, M. Ellis, H. Yang, O.G. Ziogos, S. Ghosh, J. Blumberger, *Nat. Commun.* 10 (2019) 3843.
- [8] S. Hutsch, M. Panhans, F. Ortmann, *NPJ Comput. Mater.* 8 (2022) 228.
- [9] S. Li, R. Nishikubo, T. Wada, T. Umeyama, H. Imahori, A. Saeki, *Polym. J. (Tokyo, Jpn.)* 55 (2022) 463–476.
- [10] J. Wang, X. Jiang, H. Wu, G. Feng, H. Wu, J. Li, Y. Yi, X. Feng, Z. Ma, W. Li, K. Vandewal, Z. Tang, *Nat. Commun.* 12 (2021) 6679.
- [11] C. Wöpke, C. Göhler, M. Saladina, X. Du, L. Nian, C. Greve, C. Zhu, K.M. Yallum, Y. J. Hofstetter, D. Becker-Koch, N. Li, T. Heumüller, I. Milekhin, D.R.T. Zahn, C. J. Brabec, N. Banerji, Y. Vaynzof, E.M. Herzig, R.C.I. MacKenzie, C. Deibel, *Nat. Commun.* 13 (2022) 3786.
- [12] C. He, Z. Chen, T. Wang, Z. Shen, Y. Li, J. Zhou, J. Yu, H. Fang, Y. Li, S. Li, X. Lu, W. Ma, F. Gao, Z. Xie, V. Coropceanu, H. Zhu, J.-L. Bredas, L. Zuo, H. Chen, *Nat. Commun.* 13 (2022) 2598.
- [13] S. Liu, J. Yuan, W. Deng, M. Luo, Y. Xie, Q. Liang, Y. Zou, Z. He, H. Wu, Y. Cao, *Nat. Photonics* 14 (2020) 300–305.

- [14] G.-J.A.H. Wetzelaer, N.J. Van der Kaap, L.J.A. Koster, P.W.M. Blom, *Adv. Energy Mater.* 3 (2013) 1130–1134.
- [15] S. Zeiske, O.J. Sandberg, N. Zarrabi, W. Li, P. Meredith, A. Armin, *Nat. Commun.* 12 (2021) 3603.
- [16] J. Fu, P.W.K. Fong, H. Liu, C.-S. Huang, X. Lu, S. Lu, M. Abdelsamie, T. Kodalle, C. M. Sutter-Fella, Y. Yang, G. Li, *Nat. Commun.* 14 (2023) 1760.
- [17] Y. Zhang, K. Liu, J. Huang, X. Xia, J. Cao, G. Zhao, P.W.K. Fong, Y. Zhu, F. Yan, Y. Yang, X. Lu, G. Li, *Nat. Commun.* 12 (2021) 4815.
- [18] J. Wang, Y. Wang, P. Bi, Z. Chen, J. Qiao, J. Li, W. Wang, Z. Zheng, S. Zhang, X. Hao, J. Hou, *Adv. Mater.* 35 (2023) 2301583.
- [19] K. Sivula, *ACS Energy Lett.* 7 (2022) 2102–2104.
- [20] A. Rose, *Phys. Rev.* 97 (1955) 1538–1544.
- [21] M.A. Lampert, *Phys. Rev.* 103 (1956) 1648–1656.
- [22] P. Mark, W. Helffrich, *J. Appl. Phys.* 33 (2004) 205–215.
- [23] J.A. Rohr, R.C.I. MacKenzie, *J. Appl. Phys.* 128 (2020) 128.
- [24] M. Sajedi Alvar, P.W.M. Blom, G.-J.A.H. Wetzelaer, *Nat. Commun.* 11 (2020) 4023.
- [25] J. Frenkel, *Phys. Rev.* 54 (1938) 647–648.
- [26] Y. Bai, C. Zhao, Q. Guo, J. Zhang, S. Hu, J. Liu, T. Hayat, A. Alsaedi, Z. a Tan, *Org. Electron.* 68 (2019) 168–175.
- [27] H.K.H. Lee, K.K.H. Chan, S.K. So, *Org. Electron.* 13 (2012) 541–544.
- [28] J. Yao, B. Qiu, Z.G. Zhang, L. Xue, R. Wang, C. Zhang, S. Chen, Q. Zhou, C. Sun, C. Yang, M. Xiao, L. Meng, Y. Li, *Nat. Commun.* 11 (2020) 2726.
- [29] J.A. Rohr, D. Moia, S.A. Haque, T. Kirchartz, J. Nelson, *J. Phys. Condens Matter* 30 (2018) 105901.
- [30] T. Okachi, T. Nagase, T. Kobayashi, H. Naito, *Thin Solid Films* 517 (2008) 1331–1334.
- [31] M.-J. Tsai, H.-F. Meng, *J. Appl. Phys.* 97 (2005).
- [32] J. Dacuña, A. Salleo, *Phys. Rev. B* 84 (2011) 195209.
- [33] M.C. Heiber, K. Kister, A. Baumann, V. Dyakonov, C. Deibel, T.-Q. Nguyen, *Phys. Rev. Appl.* 8 (2017) 054043.
- [34] L. Perdigón-Toro, H. Zhang, A. Markina, J. Yuan, S.M. Hosseini, C.M. Wolff, G. Zuo, M. Stolterfoht, Y. Zou, F. Gao, D. Andrienko, S. Shoaei, D. Neher, *Adv. Mater.* 32 (2020) 1906763.
- [35] X. Zhu, K. Wang, J. He, L. Zhang, H. Yu, D. He, B. Hu, *J. Phys. Chem. C* 123 (2019) 20691–20697.
- [36] K.K. Tsung, S.K. So, *J. Appl. Phys.* 106 (2009).
- [37] K.K.H. Chan, S.W. Tsang, H.K.H. Lee, F. So, S.K. So, *Org. Electron.* 13 (2012) 850–855.
- [38] C. Zhang, S. Mahadevan, J. Yuan, J.K.W. Ho, Y. Gao, W. Liu, H. Zhong, H. Yan, Y. Zou, S.-W. Tsang, S.K. So, *ACS Energy Lett.* 7 (2022) 1971–1979.
- [39] C. Kaiser, O.J. Sandberg, N. Zarrabi, W. Li, P. Meredith, A. Armin, *Nat. Commun.* 12 (2021) 3988.
- [40] W.F. Pasveer, J. Cottaar, C. Tanase, R. Coehoorn, P.A. Bobbert, P.W.M. Blom, D. M. de Leeuw, M.A.J. Michels, *Phys. Rev. Lett.* 94 (2005) 206601.
- [41] S. Fratini, M. Nikolka, A. Salleo, G. Schweicher, H. Sirringhaus, *Nat. Mater.* 19 (2020) 491–502.
- [42] R. Noriega, J. Rivnay, K. Vandewal, F.P.V. Koch, N. Stingelin, P. Smith, M. F. Toney, A. Salleo, *Nat. Mater.* 12 (2013) 1038–1044.
- [43] A. Abutaha, P. Kumar, E. Yildirim, W. Shi, S.-W. Yang, G. Wu, K. Hippalgaonkar, *Nat. Commun.* 11 (2020) 1737.
- [44] R. Noruzi, E. Lim, B.S.S. Pokuri, M.L. Chabiny, B. Ganapathysubramanian, *NPJ Comput. Mater.* 8 (2022) 38.
- [45] W. Zhang, C. Sun, I. Angunawela, L. Meng, S. Qin, L. Zhou, S. Li, H. Zhuo, G. Yang, Z.-G. Zhang, H. Ade, Y. Li, *Adv. Mater.* 34 (2022) 2108749.
- [46] M. Zhang, L. Zhu, G. Zhou, T. Hao, C. Qiu, Z. Zhao, Q. Hu, B.W. Larson, H. Zhu, Z. Ma, Z. Tang, W. Feng, Y. Zhang, T.P. Russell, F. Liu, *Nat. Commun.* 12 (2021) 309.
- [47] X. Zhang, C. Li, J. Xu, R. Wang, J. Song, H. Zhang, Y. Li, Y.-N. Jing, S. Li, G. Wu, J. Zhou, X. Li, Y. Zhang, X. Li, J. Zhang, C. Zhang, H. Zhou, Y. Sun, Y. Zhang, *Joule* 6 (2022) 444–457.
- [48] K. Weng, L. Ye, L. Zhu, J. Xu, J. Zhou, X. Feng, G. Lu, S. Tan, F. Liu, Y. Sun, *Nat. Commun.* 11 (2020) 2855.
- [49] H. Tang, T. Xu, C. Yan, J. Gao, H. Yin, J. Lv, R. Singh, M. Kumar, T. Duan, Z. Kan, S. Lu, G. Li, *Adv. Sci.* 6 (2019) 1901613.
- [50] J. Wang, C. Han, S. Wen, F. Bi, Z. Hu, Y. Li, C. Yang, X. Bao, J. Chu, *Energy Environ. Sci.* 16 (2023) 2327–2337.
- [51] G. Li, V. Shrotriya, J. Huang, Y. Yao, T. Moriarty, K. Emery, Y. Yang, *Nat. Mater.* 4 (2005) 864–868.
- [52] C.H.Y. Ho, Y. Pei, Y. Qin, C. Zhang, Z. Peng, I. Angunawela, A.L. Jones, H. Yin, H. F. Iqbal, J.R. Reynolds, K. Gundogdu, H. Ade, S.K. So, F. So, *ACS Appl. Mater. Interfaces* 14 (2022) 47961–47970.
- [53] X. Du, X. Li, H. Lin, L. Zhou, C. Zheng, S. Tao, *J. Mater. Chem. A* 7 (2019) 7437.
- [54] P. Cheng, C. Yan, T.-K. Lau, J. Mai, X. Lu, X. Zhan, *Adv. Mater.* 28 (2016) 5822.
- [55] Y. Zhang, K. Liu, J. Huang, X. Xia, J. Cao, G. Zhao, P.W.K. Fong, Y. Zhu, F. Yan, Y. Yang, X. Lu, G. Li, *Nat. Commun.* 12 (2021) 4815.
- [56] R. Zeng, L. Zhu, M. Zhang, W. Zhong, G. Zhou, J. Zhuang, T. Hao, Z. Zhou, L. Zhou, N. Hartmann, X. Xue, H. Jing, F. Han, Y. Bai, H. Wu, Z. Tang, Y. Zou, H. Zhu, C.-C. Chen, Y. Zhang, F. Liu, *Nat. Commun.* 14 (2023) 4148.
- [57] Z. Fu, T. Wang, W.-Q. Zhang, J.-W. Qiao, F.-Z. Cui, H. Yin, X.-Y. Du, Q. Wei, X.-T. Hao, *PRX, Energy* 2 (2023) 043012.
- [58] R. Yu, H. Yao, L. Hong, Y. Qin, J. Zhu, Y. Cui, S. Li, J. Hou, *Nat. Commun.* 9 (2018) 4645.
- [59] Z. Ge, J. Qiao, Y. Li, J. Song, C. Zhang, Z. Fu, M.H. Jee, X. Hao, H.Y. Woo, Y. Sun, *Adv. Mater.* 35 (2023) 2301906.
- [60] Y. Wu, Q. Fan, B. Fan, F. Qi, Z. Wu, F.R. Lin, Y. Li, C.-S. Lee, H.Y. Woo, H.-L. Yip, A. K.Y. Jen, *ACS Energy Lett.* 7 (2022) 2196.

Dongcheng Jiang is currently working toward a Master's degree in Physics supervised by Prof. Hang Yin at School of Physics, Shandong University. His research focuses on the study of charge carrier transport in organic semiconductors.



Jiangkai Sun is a Master degree candidate in Physics under the supervision of Prof. Hang Yin at Shandong University. His current research focuses on the study of charge carrier transport in organic semiconductors.



Ruijie Ma is currently a Postdoctoral Research Scholar in Department of Electrical and Electronic Engineering, the Hong Kong Polytechnic University. He received his PhD degree in the Department of Chemistry, Hong Kong University of Science and Technology. His research's mainly about organic solar cells.



Vox Kalai Wong is an experimental physicist who specializes in studying a wide range of physical and chemical properties of semiconducting materials, with a particular emphasis on organic and perovskite materials. She has a strong research interest in investigating the optical, electrical, thermal, morphological, and topological properties of organic photovoltaics.



Jianyu Yuan is a Professor in Materials Science and Engineering, Soochow University. His research interests are design and synthesis of functional conjugated materials for photovoltaic application, high-efficiency and stable perovskite solar cells, design and synthesis of functional nanocrystals for photovoltaic application, and organic/nanocrystal hybrid materials for photovoltaic application. Prof. Yuan has over 160 SCI papers, and the total citation times of his papers are over 7500 with H-index of 50 (based on Google Scholar).





Kun Gao is an Associate Professor in School of Physics, Shandong University. His research interests focus on the theoretical modeling and exciton physics, in particular organic semiconductors with optoelectronic and spintronic applications. He obtained MS and PhD degrees from Shandong University. Prof. Gao has more than 70 papers published in peer-reviewed journals, 2 professional books.



Xiaotao Hao is currently a Professor at the School of Physics in Shandong University, China. He holds the titles of Fellow of the Institute of Physics (FInstP) and Fellow of the Royal Society of Chemistry (FRSC). Before returning to China, he worked at various research institutions in Australia, Japan, and Singapore. His current research focuses on the physics of organic optoelectronic materials and devices, as well as ultrafast spectroscopy and microscopy.



Feng Chen is a Distinguished Professor at Shandong University, China. He received the PhD from Shandong University in 2002. His research interests include fabrication of micro-nanoscale photonic structures, ultrafast laser writing, ion beam modification of nanomaterials, lasers, etc. He has more than 400 papers published in peer-reviewed journals, 1 professional book, 5 book chapters, and holds 10 patents. He is a Fellow of Institute of Physics (IOP UK), OPTICA (formerly OSA), and SPIE.



Gang Li is a Professor in the Department of Electrical and Electronic Engineering, the Hong Kong Polytechnic University. His research interests are the materials, device engineering and device physics in organic semiconductors and hybrid perovskite semiconductors, focusing on energy applications. He obtained his BS degree in Space Physics from Wuhan University (China), MS in Electrical Engineering and PhD in Condensed Matter Physics from Iowa State University (USA). He was a research professor in UCLA, and VP of Solarmer Energy Inc. He has been a Thomson Reuters/Clarivate Analytics Highly Cited Researcher since 2014, across the categories of Materials Science, Physics and Chemistry. He has published ~180 papers, with over 70k citations. He is Optica Fellow (Former OSA Fellow), Fellow of Royal Society of Chemistry (RSC), and The International Society for Optics and Photonic (SPIE).



Shu Kong So obtained his bachelor degree from Hamilton College and PhD in Physics from Cornell University. In Cornell, he did research on surface physics and chemistry of small molecules on metal and semiconductor surfaces. He was a postdoctoral fellow in the Chemistry Department of the University of Toronto where he used scanning tunneling microscope to study surface photochemistry. In 1992, he joined the Department of Physics, Hong Kong Baptist University. Now he is the Acting Head and a Professor of Physics. His major research interest is in the physics and the chemistry of thin film materials including transport and defect study of organic films, fabrication of organic solar cells and thin film transistors, surface and optical spectroscopies of materials, and pulsed

laser deposition.



Hang Yin is a Professor working at School of Physics in Shandong University, China. He obtained BS degree from Qufu Normal University, MS and PhD degrees from Hong Kong Baptist University. He was a postdoctoral fellow in Hong Kong Baptist University and the Hong Kong Polytechnic University. His current research interests are charge carrier transport and film defect analysis of organic semiconductors.

Supplementary material

Extracting charge carrier mobility in organic solar cells through space-charge-limited current measurements

Authors: Dongcheng Jiang,¹ Jiangkai Sun,¹ Ruijie Ma,² Vox Kalai Wong,³ Jianyu Yuan,⁴ Kun Gao,¹ Feng Chen,¹ Shu Kong So,³ Xiaotao Hao,¹ Gang Li,² Hang Yin^{1*}

Affiliations:

¹School of Physics, State Key Laboratory of Crystal Materials, Shandong University; Jinan, 250100, P. R. China.

²Department of Electrical and Electronic Engineering, Research Institute for Smart Energy (RISE), Photonic Research Institute (PRI), The Hong Kong Polytechnic University, Kowloon, Hong Kong SAR 999077, PR China

³Department of Physics and Institute of Advanced Materials, Hong Kong Baptist University; Kowloon Tong, Hong Kong SAR, 999077 P. R. China.

⁴Institute of Functional Nano & Soft Materials (FUNSOM), Soochow University; Suzhou, 215123, P. R. China.

* Corresponding author. Email: hyin@sdu.edu.cn.

Supplementary Text

Space-charge-limited current model

Space charge refers to the accumulation of charges in a particular region, which influences the charge particle flow. The space charge and the concomitant push-back electrostatic field strongly influence the charge particle flow that injected in give rise to the space-charge-limited current (SCLC) [1]. The current density-voltage (J - V) response of an organic semiconductor can be described by the SCLC model. Poisson's equation can be used to describe the electric field (F) dependent spatial (x) charge distribution:

$$\frac{\partial F}{\partial x} = \frac{q\rho}{\epsilon_r \epsilon_0} \quad (1.1)$$

$$-\frac{1}{q} J_n = -D_n \frac{dn}{dx} + n_f \mu_n F \quad (1.2)$$

$$\frac{1}{q} J_p = -D_p \frac{dp}{dx} - p_f \mu_p F \quad (1.3)$$

Where ρ is the total space charge density, $\epsilon_0 \epsilon_r$ is the permittivity, q is the elementary charge, J_n and J_p are the current density for electron and hole respectively, D_n and D_p are the diffusion coefficients, n_f and p_f are the free charge carrier density, and μ_n and μ_p are the charge carrier mobilities.

The total space charge density is given by the sum if all charge carriers present in the device,

$$\rho = q (p_f - n_f + p_t - n_t + N_D^+ - N_A^-) \quad (1.4)$$

Where p_t and n_t represent the localized charge carrier density in trap states, and N_D^+ and N_A^- are the free charge carriers due to ionized donor and acceptor states. Moreover, the total space charge density contributes to the overall electrostatic potential, only the free charge carriers, p_f , n_f , N_D^+ and N_A^- , contribute to the current density.

Throughout the discussion of the SCLC model, the simplified SCLC model will be considered. The simplified theory relies on two assumptions: a) neglecting diffusion current. b) the semiconductor is sandwiched between two ohmic contacts.

1.1 Mott-Gurney model

The Mott-Gurney (MG) model describes current flow transport in semiconductors that are free of traps, doping, and energetic disorder, in response to an applied voltage [2]:

$$\frac{\partial F}{\partial x} = -\frac{en_f}{\epsilon_r \epsilon_0} \quad (1.5)$$

$$J_n = -qn(x)\mu_n F(x) \quad (1.6)$$

The boundary condition for spatial positions can assume that electric field at boundary $F(0) = 0$. From the above two equation can be integrated as:

$$J \int_0^x dx = - \int_0^F \mu_n \epsilon_r \epsilon_0 F(x) dF(x) \quad (1.7)$$

Since the current across the device is in steady states, the current density J is a constant. From Eq. 1.8 the expression for electric field distribution can be obtained,

$$F = -\sqrt{\frac{2Jx}{\mu_n \epsilon_r \epsilon_0}} \quad (1.8)$$

The expression for current density as a function of voltage can be derived as follows:

$$V = \int_0^L F dx = -\left(\frac{8J}{9\mu_n \epsilon_0 \epsilon_r}\right)^{1/2} L^{3/2} \quad (1.9)$$

which upon rearrangement yields the MG model,

$$J = \frac{9}{8} \mu_n \epsilon_r \epsilon_0 \frac{V^2}{L^3} \quad (1.10)$$

* Diffusion contribution of the MG model

The simplified SCLC model assumed that the contribution of the diffusion current should be neglected. However, the carrier density gradient calculated using Gauss theorem will give rise to the diffusion current. The contribution of the diffusion current can approximately calculate,

$$n = \frac{1}{q} \sqrt{\frac{J \epsilon_r \epsilon_0}{2 \mu_n x}} \quad (1.11)$$

$$J_{\text{diffusion}} \approx qD \frac{dn}{dx} = D \frac{d}{dx} \sqrt{\frac{J_{\text{drift}} \epsilon_r \epsilon_0}{2 \mu_n x}} = -D \frac{3}{8} \frac{\epsilon_r \epsilon_0 V}{(xL)^{3/2}} \quad (1.12)$$

By incorporating Einstein Relation $D = \mu k_B T / q$, the ratio of diffusion to drift current can be obtained,

$$\left| \frac{J_{\text{diffusion}}}{J_{\text{drift}}} \right| = \frac{k_B T}{3qV} \left(\frac{x}{L} \right)^{-3/2} \quad (1.13)$$

1.2 Rose and Lampert model

The Rose and Lampert (RL) model elucidates the behavior of carriers hindered by deep

discrete traps located in the mid-gap [3, 4]. Boltzmann statistics can be adopted to describe both the populations of free carriers (n_f) and trapped carriers (n_t), when the Fermi level lies in more than $2k_B T$ below the trap level.

$$n_f = N_c \exp\left(\frac{E_F - E_C}{k_B T}\right) \quad (1.14)$$

$$n_t = N_t \exp\left(\frac{E_F - E_t}{k_B T}\right) \quad (1.15)$$

Here, N_C and N_t represent the densities of charge carriers and traps, respectively. The parameter θ is introduced to describe the ratio of concentration of charge carriers and traps.

$$\theta = \frac{n_f}{n_t} = \frac{N_C}{N_t} \exp\left(-\frac{E_C - E_t}{k_B T}\right) \quad (1.16)$$

The Poisson's equation can be written as ($n_t \gg n_f$),

$$\frac{dF}{dx} = \frac{n_f + n_t}{\epsilon_0 \epsilon_r} \approx \frac{n_t}{\epsilon_0 \epsilon_r} \quad (1.17)$$

The expression for current density becomes,

$$J = \mu_n \theta \epsilon F \frac{dF}{dx} \quad (1.18)$$

$$\int_0^x \frac{J}{\mu \epsilon \theta} dx = \int_{F(0)}^{F(x)} F dx \quad (1.19)$$

Noting the boundary condition $F(0) = 0$,

$$F(x) = \left(\frac{2Jx}{\mu \epsilon \theta} \right)^{1/2} \quad (1.20)$$

$$V = \int_0^L F(x) dx = \left(\frac{8J}{9\mu \epsilon \theta} \right)^{1/2} L^{3/2} \quad (1.21)$$

The RL model shown as:

$$J = \frac{9}{8} \mu \epsilon \frac{V^2}{L^3} \frac{N_C}{N_t} \exp\left(-\frac{E_C - E_t}{k_B T}\right) \quad (1.22)$$

1.3 Mark and Helfrich model

The Mark-Helfrich (MH) model describes current flow transport in semiconductors with the exponential tail of states extending into the conduction band edge [5]:

$$n_t(E) = \frac{N_t}{k_B T_c} \exp\left(-\frac{E}{k_B T_c}\right) \quad (1.23)$$

where N_t is the total trap density and T_c is the characteristic temperature of the tails. At $T=0$ K, it can be assumed that all of the space-charge are in the traps and the trap states will be filled up to the quasi-Fermi level,

$$\rho(x_0) = q \int_{-\infty}^{E_F} \frac{N_t}{E_{ch}} \exp\left(-\frac{E(x_0)}{E_{ch}}\right) dE \quad (1.24)$$

If the temperature above 0 K, some charge carriers are allowed to escape the trap states, and these free charge carriers are given by Boltzmann statistics as,

$$\rho_f(x_0) = q N_C \exp(-E_F(x_0)/k_B T) \quad (1.25)$$

We can combine the above expressions for the total space-charge density, $\rho(x_0)$, and the free charge carrier density, $\rho_f(x_0)$, to yield,

$$\rho_f = N_C q^{1-l} N_t^{-l} \rho^l \quad (1.26)$$

where $l = E_{ch}/k_B T$. Similar for the derivation of the MG model, we now have to solve the drift diffusion equation along with the Poisson equation.

$$J = N_C q^{1-l} N_t^{-l} \rho^l \mu F(x) \quad (1.27)$$

$$\frac{dF(x)}{dx} = \frac{N_t}{\epsilon_r \epsilon_0} q^{(l-1)/l} \left(\frac{J}{\mu N_C} \right)^{1/l} [F(x)]^{-1/l} \quad (1.28)$$

subject to the boundary condition $F(0) = 0$, we obtain

$$[F(x)]^{1/l} dF = D dx \quad (1.29)$$

The solution satisfying the boundary condition is

$$F = \left(\frac{l+1}{l} D \right)^{l/(l+1)} x^{l/(l+1)} \quad (1.30)$$

To obtain an expression in terms of the voltage, we integrate the electric field across the entire thickness of the device,

$$V = \int_0^L F dx = \left(\frac{l+1}{l} D \right)^{l/(l+1)} \int_0^L x^{l/(l+1)} dx \quad (1.31)$$

The MH model can be obtained

$$J = q^{1-l} \mu N_C \left(\frac{\epsilon_r \epsilon_0 l}{N_t (l+1)} \right)^l \left(\frac{2l+1}{l+1} \right)^{l+1} \frac{V^{l+1}}{L^{2l+1}} \quad (1.32)$$

*Diffusion contribution of MH model

Similar to the derivation of the MG model, we can obtain the diffusion contribution of the MH model,

$$\left| \frac{J_{\text{diffusion}}}{J_{\text{drift}}} \right| = \frac{k_B T}{qV} \frac{1}{l+1} \left(\frac{x}{L} \right)^{-1} \quad (1.33)$$

1.4 Poole-Frenkel Model

The Poole-Frenkel model reflects the behavior of trapped carriers released by the strong electric field. The strong electric field may reduce the effective depth of the trap, which allowed carriers to be released from the trap [6]. The relationship between the mobility and the electric field is given by

$$\mu(F) = \mu_0 \exp(0.89\beta\sqrt{F}) \quad (1.34)$$

where μ_0 implies the zero-field mobility, β is the Poole-Frenkel slope.

The Poole-Frenkel (PF) model can be formulated with MG model incorporating the field-dependent PF effect

$$J = \frac{9}{8} \varepsilon_r \varepsilon_0 \frac{V^2}{L^3} \mu_0 \exp(0.89\beta\sqrt{F}) \quad (1.35)$$

Protocol for extracting mobilities accurately using standard SCLC measurement

1) Evaluate single-carrier device structure:

- Apply a voltage higher than 1 V to disregard the influence of diffusion current.
- Check for reasonable energy levels and work functions for charge-transporting layers and electrodes to estimate the built-in field. Consider the modifying ability of widely-used interlayers (i.e., PDI derivative) for lowering electrodes work function.
- Ensure the thickness of single-carrier devices is around 200 nm to eliminate the effect of non-ohmic contact.

2) Choose appropriate differentiated SCLC models:

- Calculate the slope of current density-voltage ($J-V$) curves: $g(V) = d \ln J / d \ln V$.
- If a continuous upward trend is shown in $g(V)$ curves, the Poole-Frenkel (PF) model is suitable for numerical fitting.
- If a plateau is exhibited in the intermediate voltage region of $g(V)$ curves, use the eigenvalue of the $g(V)$ function to determine appropriate SCLC models. The average value of $g(V)$ in the platform interval represents the eigenvalue.
- If the eigenvalue is over 2, the Mark-Helfrich (MH) model for mobility extraction when the exponential tail of states hinders the flat carrier transport landscape.
- If the eigenvalue is around 2, consider either the Mott-Gurney (MG) or Rose-Lampert (RL) model. Distinguish between MG and RL models based on the slope transition in the high voltage range caused by carrier injection leading to trap filling.

3) Select data range for fitting:

- Choose a voltage range for fitting where the curve is reasonably flat and data have not been excluded in previous steps.
- Select the fitting region to include as large an interval as possible while excluding singular values. Only data points from within this range will be used for least-squares fitting.

4) Perform least-squares fitting:

- Use a least-squares fitting algorithm to fit the data according to the selected equation within the chosen range.

*Complete worked examples

1) Electron-only device:

- The built-in voltage for the single-carrier device mentioned in the Fig. S1 is determined to be 0.5 eV.

2) $g(V)$ curve analysis:

- The $g(V)$ curve exhibits three distinct regions:
 - Carrier injection rising edge in low voltage (< 1 V).
 - Relatively flat intermediate region from 1-4 V.
 - Field-dependent rising edge in high voltage (> 4 V).

3) Eigenvalue and model selection:

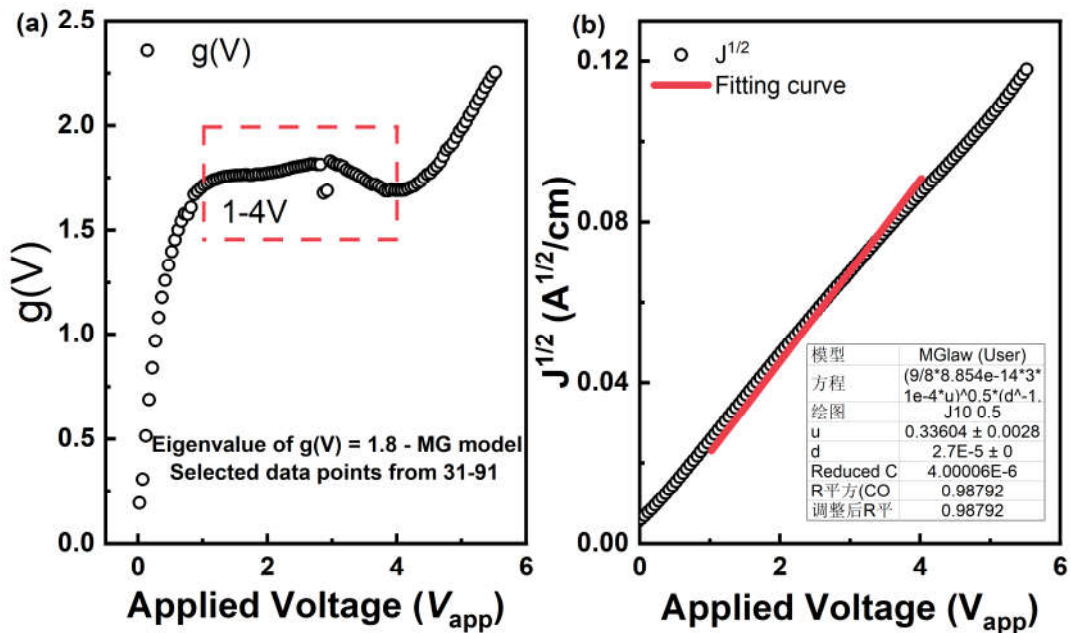
- The eigenvalue of $g(V)$ function around 2 (1.8) indicating the MG model should be employed.
- The selected fitting region is from 1 to 4V.

4) Least-squares fitting:

- The data are fitted using a least squares-fitting algorithm.

5) Mobility calculation:

- The mobility is calculated to be $3.4 \times 10^{-5} \text{ cm}^2\text{V}^{-1}\text{s}^{-1}$.



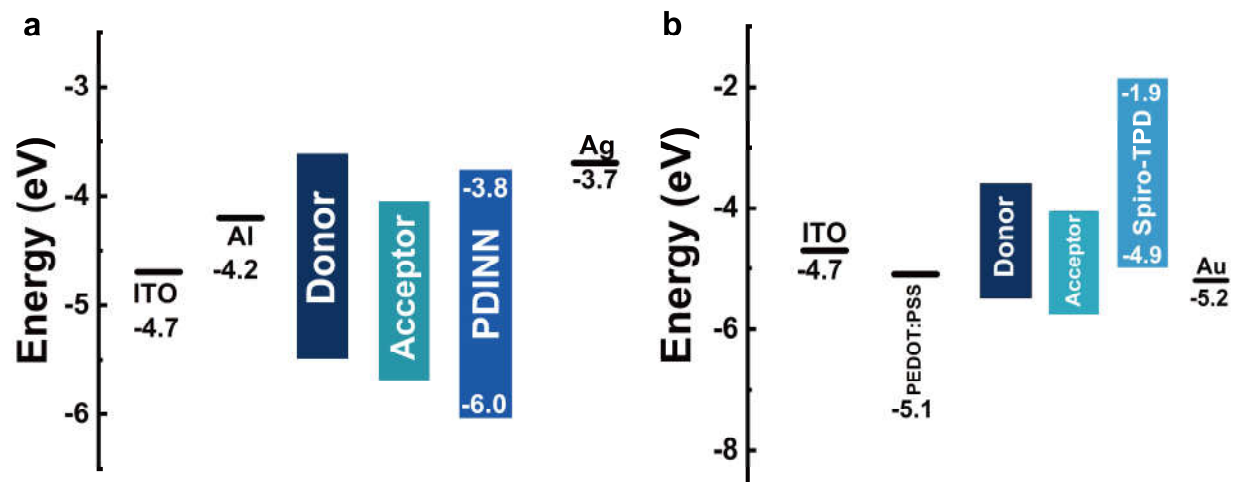


Figure S1. Single-carrier device structures for electron only (a) and hole-only (b) devices.

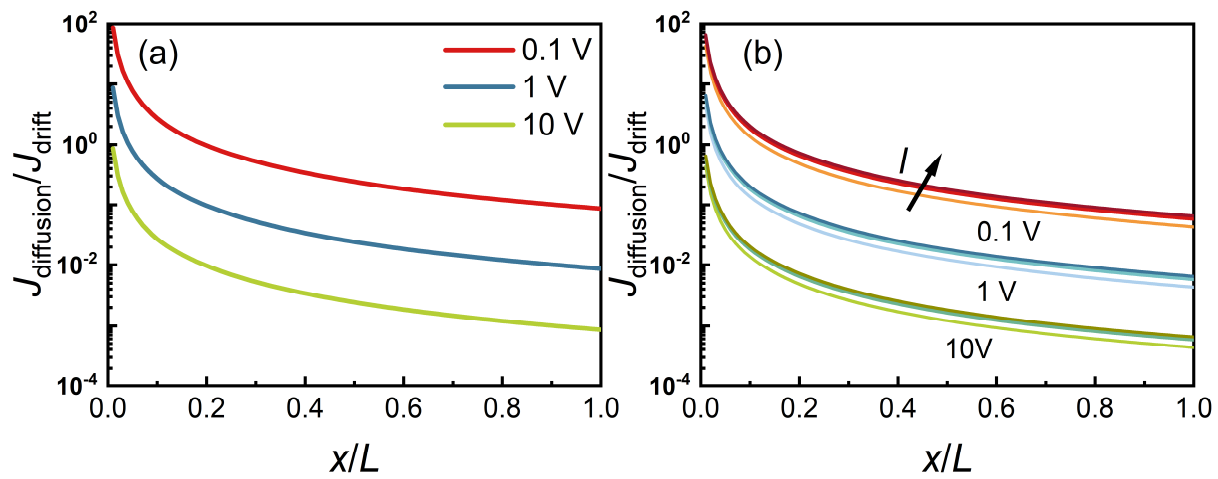


Figure S2. Ratio of diffusion current and drift current in devices at 0.1, 1 and 10V analyzed by MG model (a) and MH model (b).

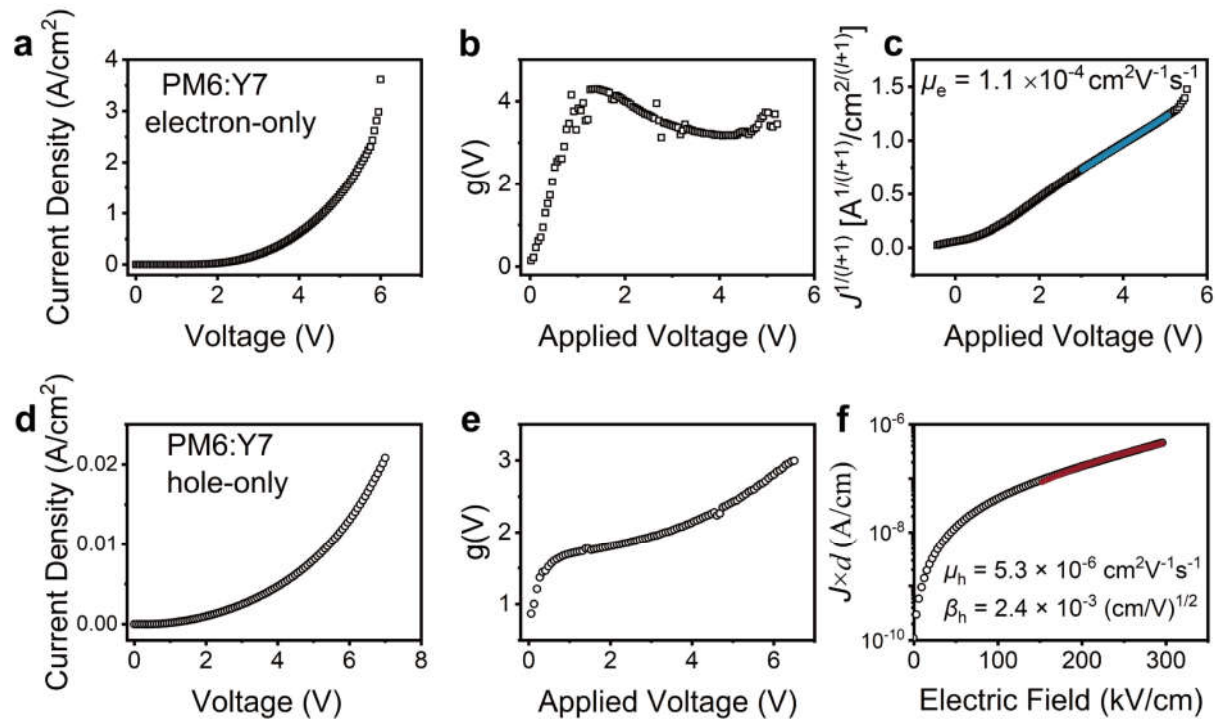


Figure S3. The J - V curve, the slope of J - V curve and mobility extraction depend on the model selection criterion in electron-only device (a-c) and hole-only device (d-f).

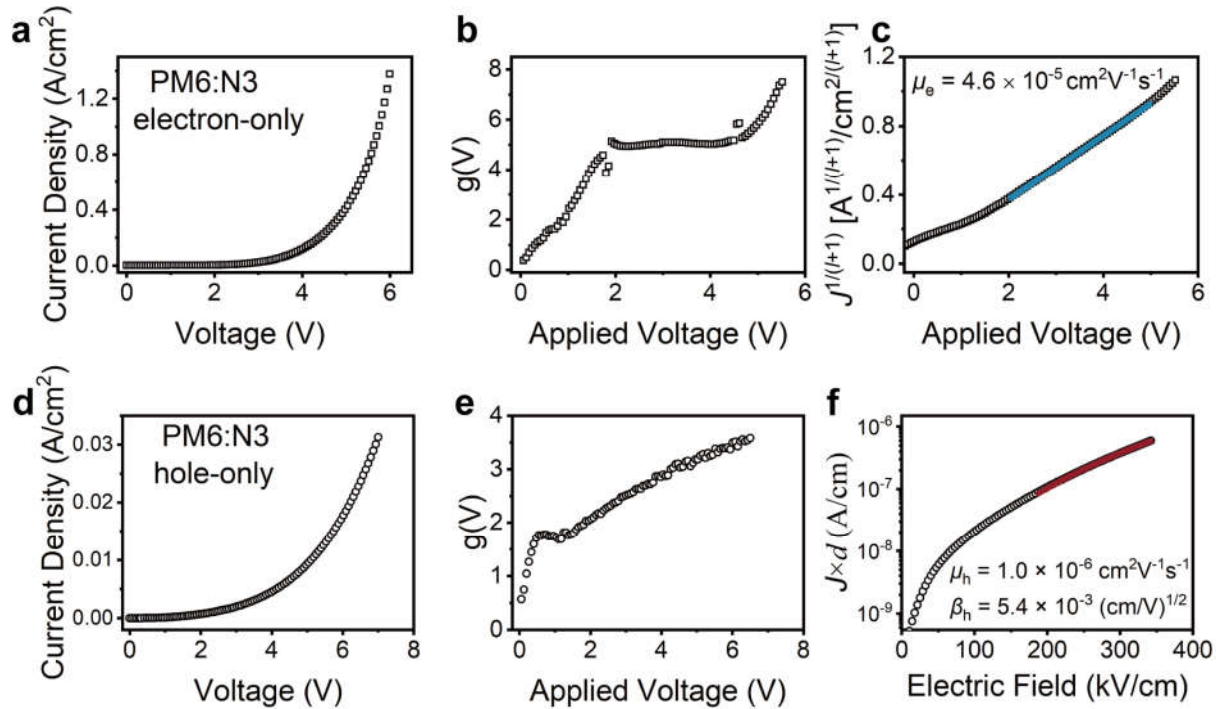


Figure S4. The J - V curve, the slope of J - V curve and mobility extraction depend on the model selection criterion in electron-only device (a-c) and hole-only device (d-f).

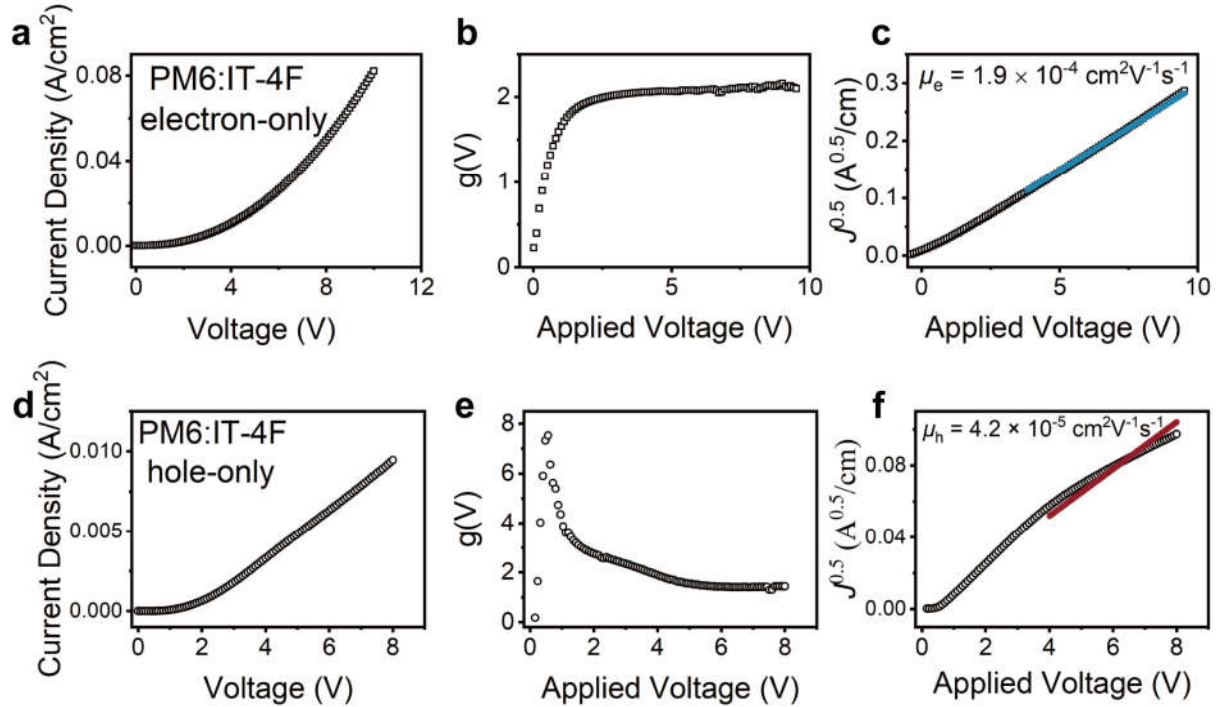


Figure S5. The J - V curve, the slope of J - V curve and mobility extraction depend on the model selection criterion in electron-only device (a-c) and hole-only device (d-f).

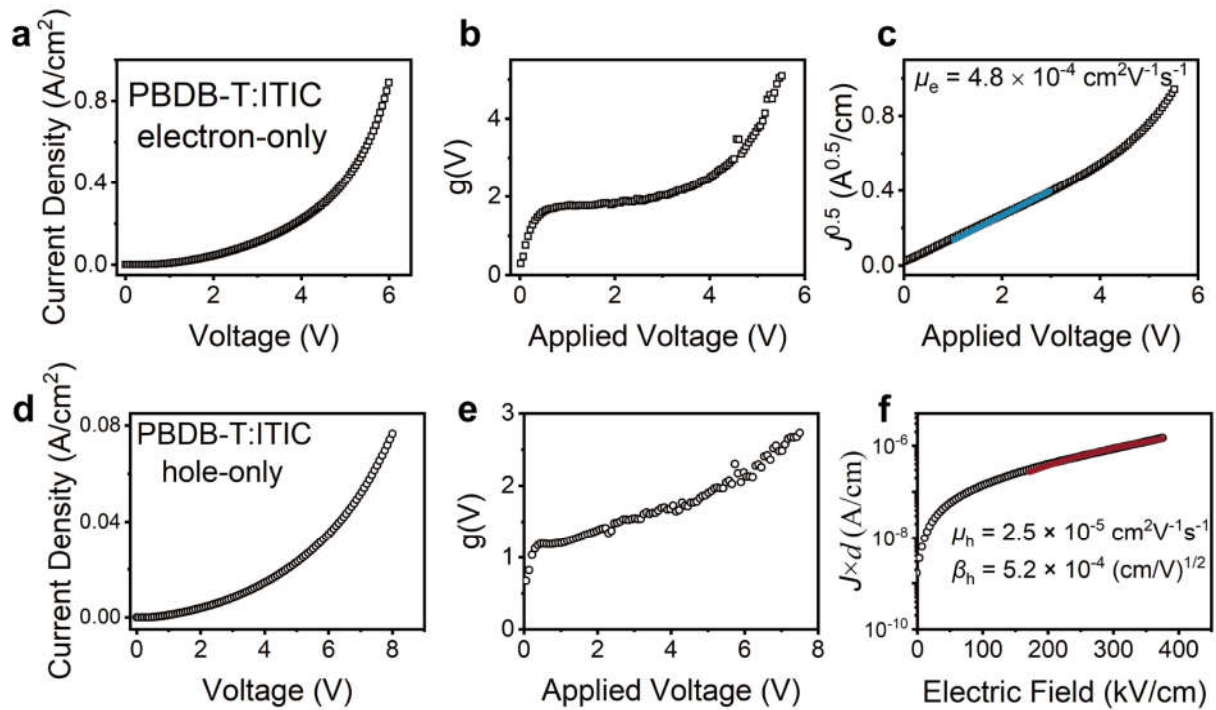


Figure S6. The J - V curve, the slope of J - V curve and mobility extraction depend on the model selection criterion in electron-only device (a-c) and hole-only device (d-f).

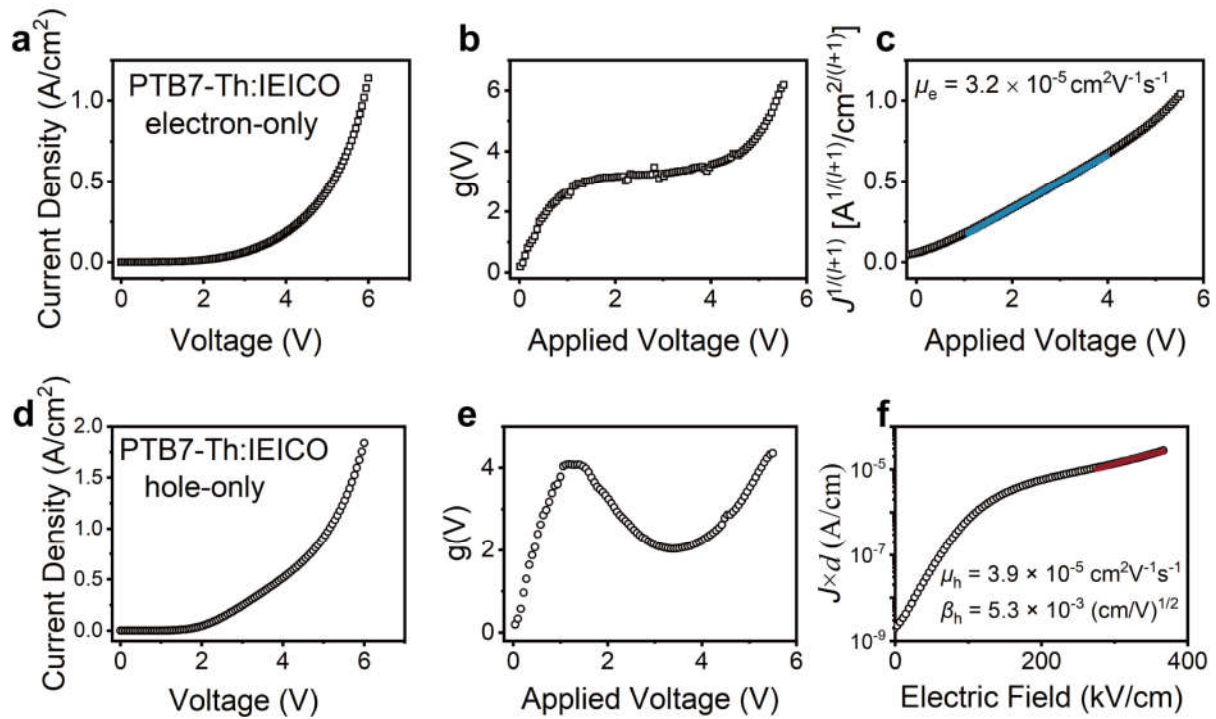


Figure S7. The J - V curve, the slope of J - V curve and mobility extraction depend on the model selection criterion in electron-only device (a-c) and hole-only device (d-f).

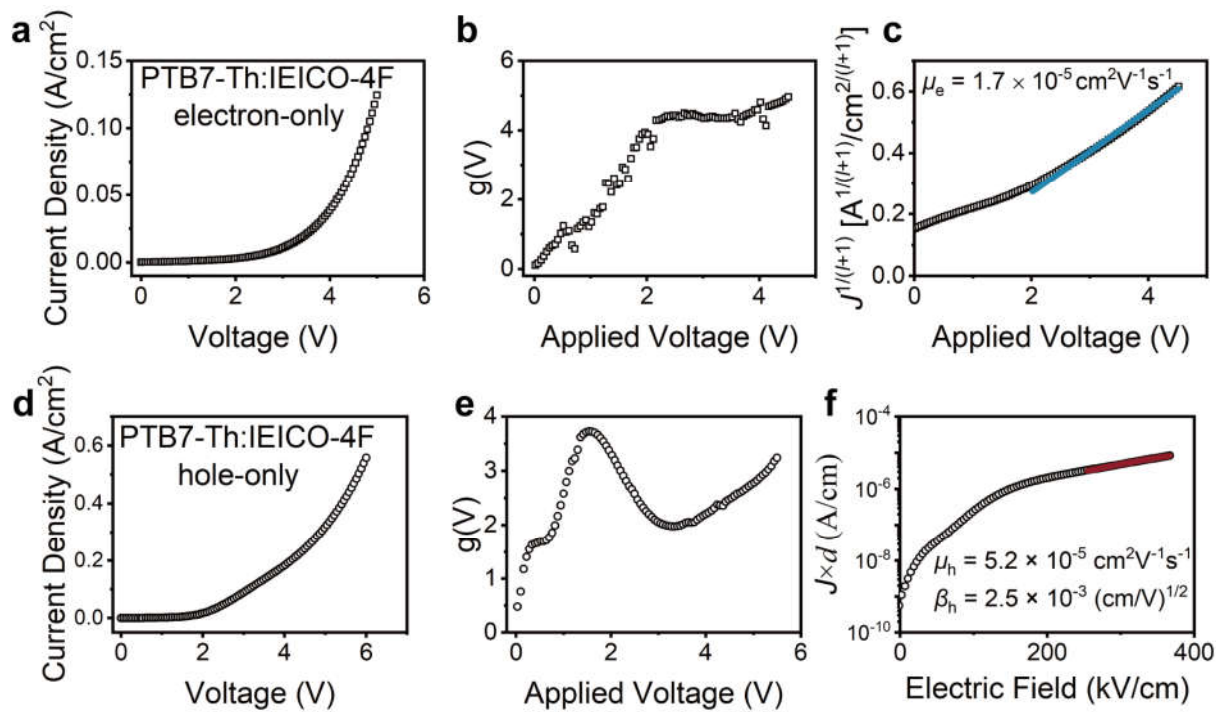


Figure S8. The J - V curve, the slope of J - V curve and mobility extraction depend on the model selection criterion in electron-only device (a-c) and hole-only device (d-f).

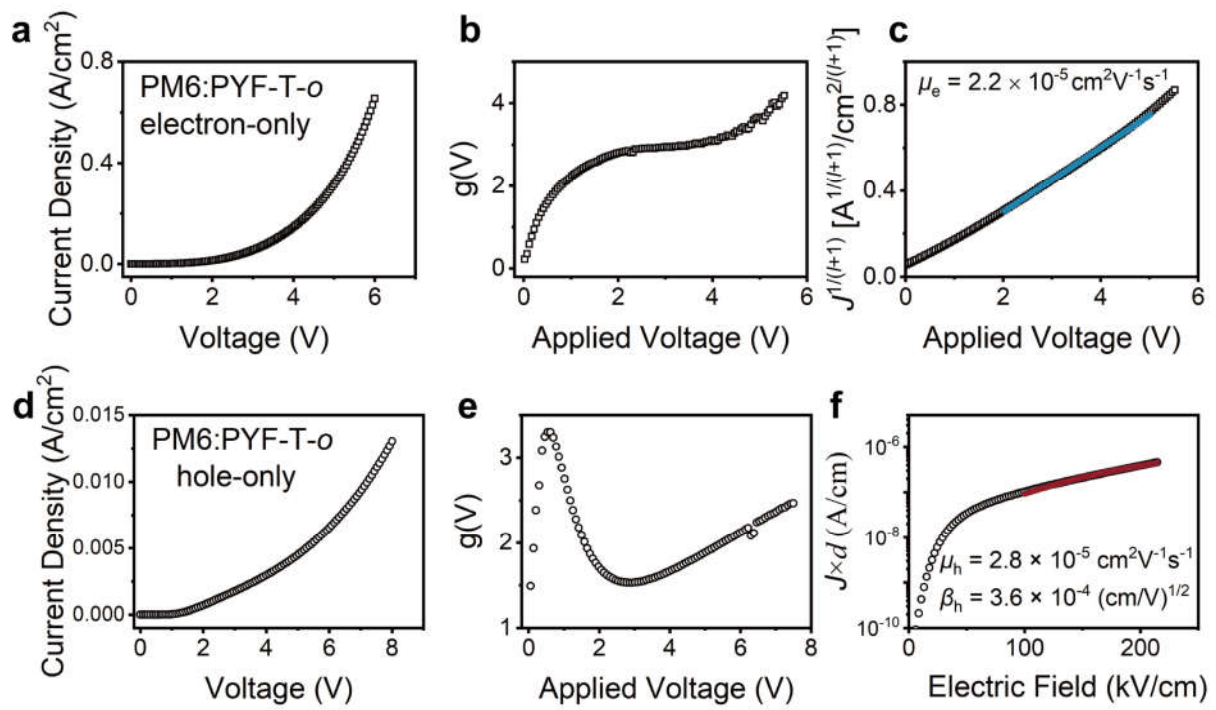


Figure S9. The J - V curve, the slope of J - V curve and mobility extraction depend on the model selection criterion in electron-only device (a-c) and hole-only device (d-f).

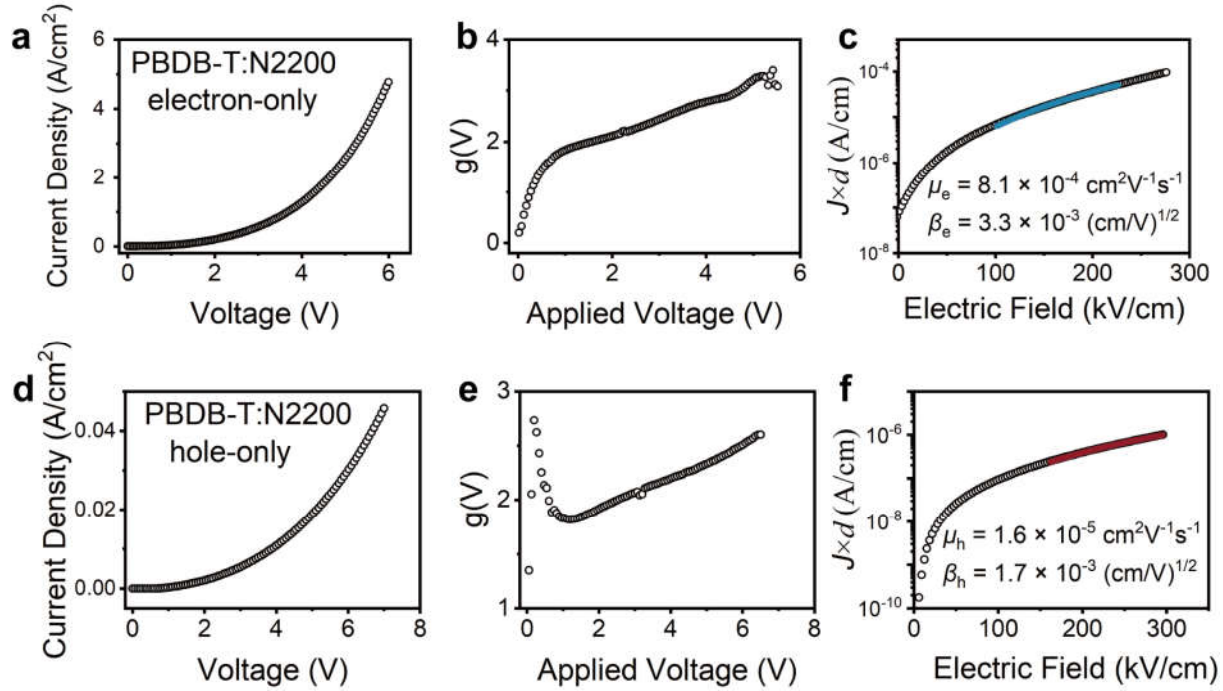


Figure S10. The J - V curve, the slope of J - V curve and mobility extraction depend on the model selection criterion in electron-only device (a-c) and hole-only device (d-f).

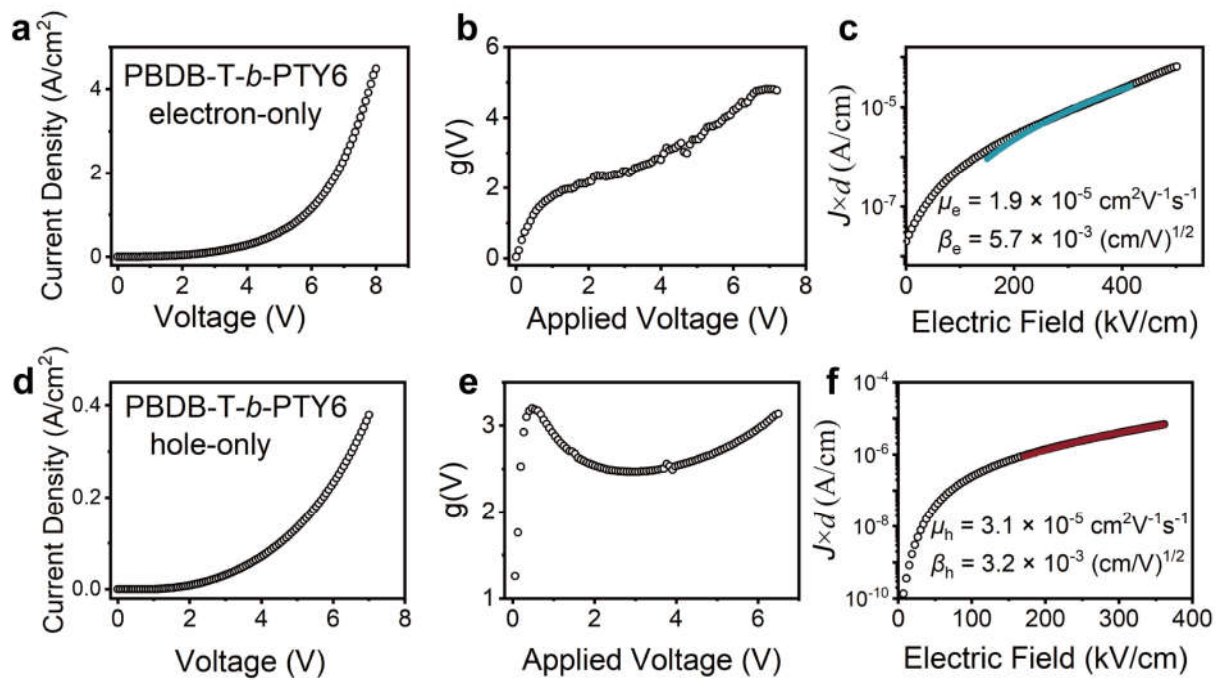


Figure S11. The J - V curve, the slope of J - V curve and mobility extraction depend on the model selection criterion in electron-only device (a-c) and hole-only device (d-f).

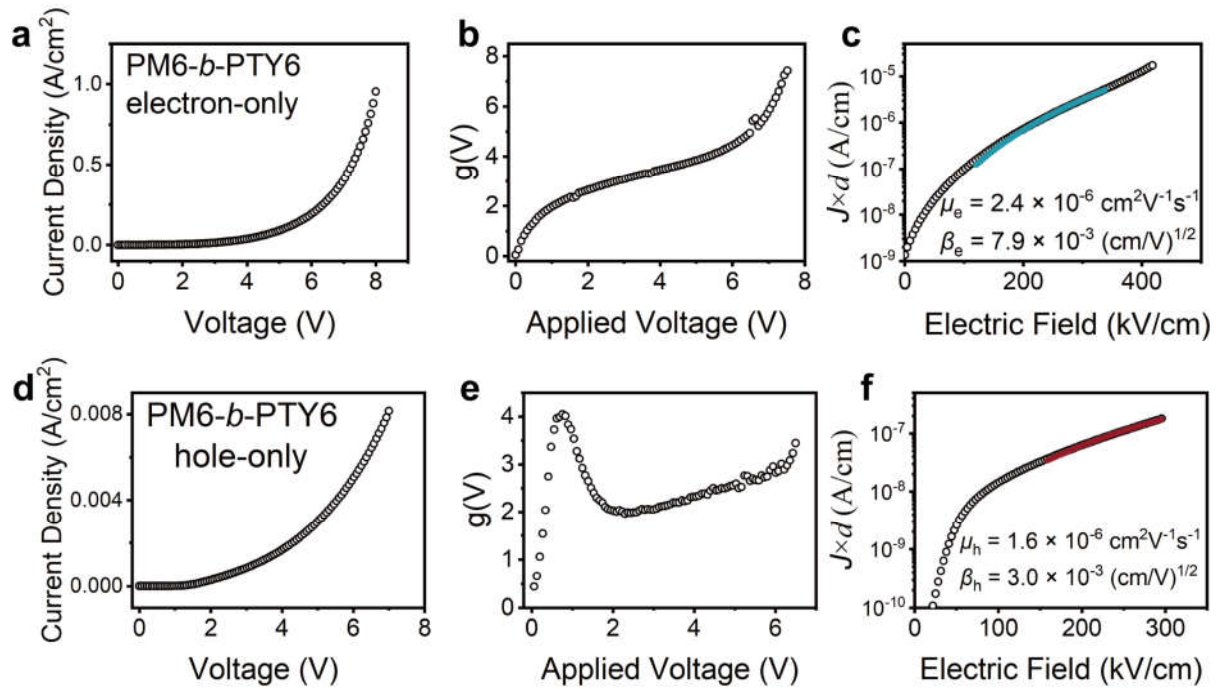


Figure S12. The J - V curve, the slope of J - V curve and mobility extraction depend on the model selection criterion in electron-only device (a-c) and hole-only device (d-f).

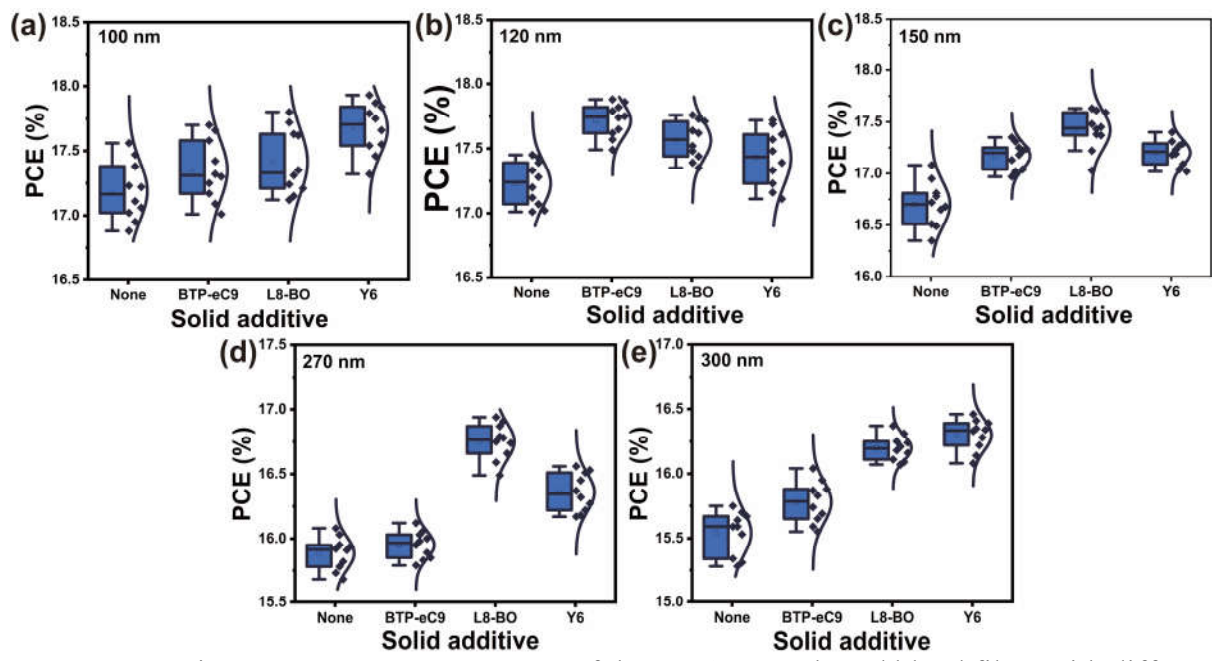


Figure S13. Histogram PCE measurements of the PM6:PY-IT based blend films with different thickness (a-e).

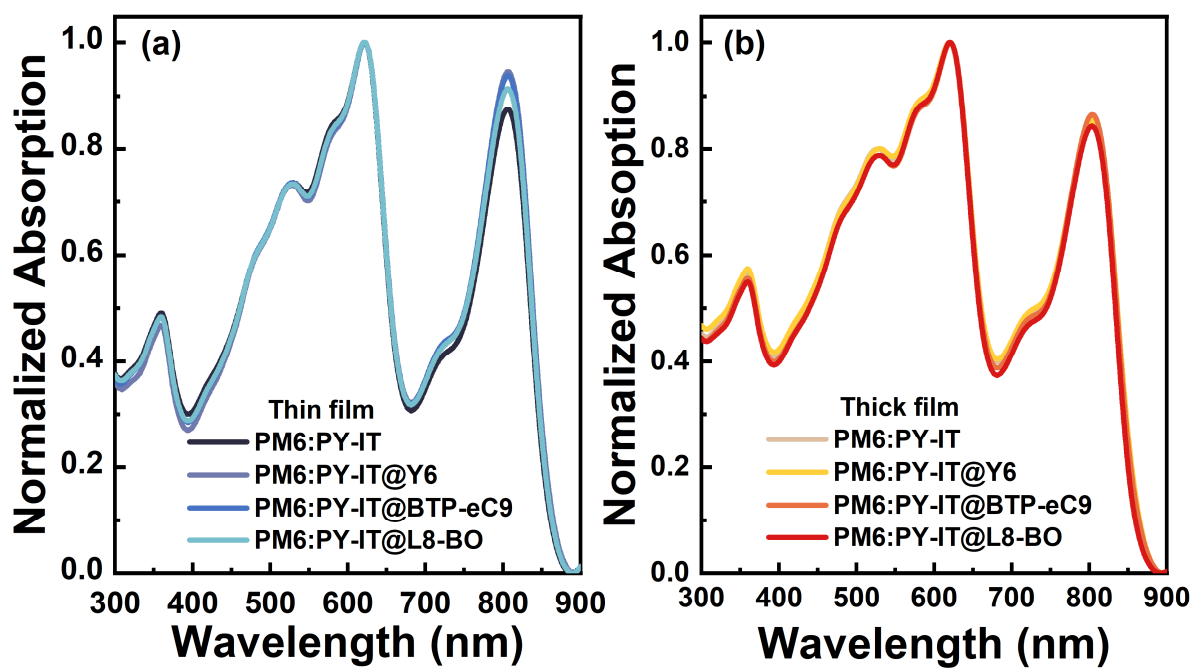


Figure S14. UV-vis absorption of a) thin and b) thick curves of the PM6:PY-IT based blend films.

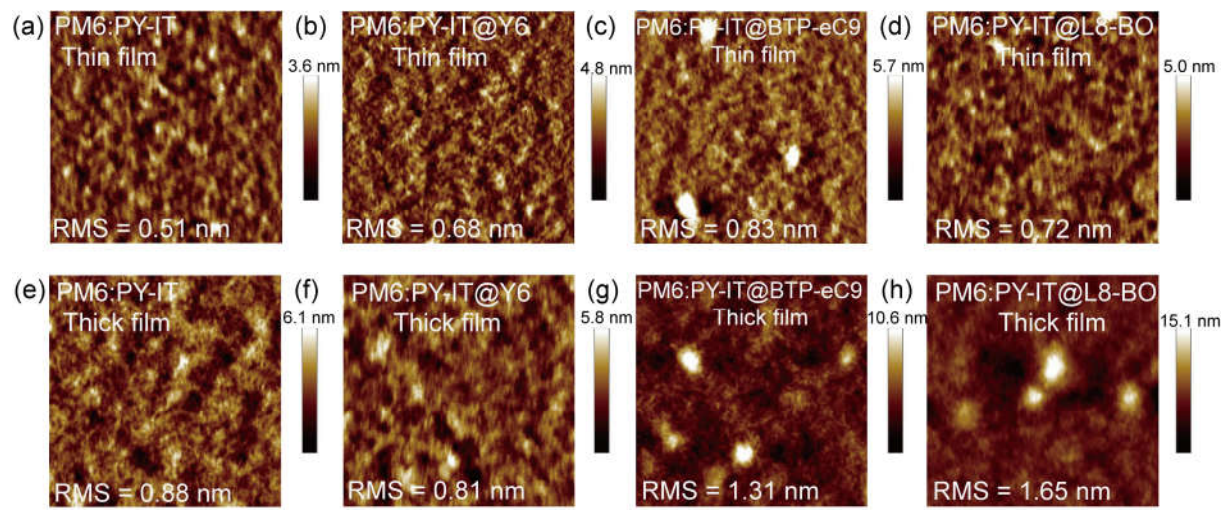


Figure S15. AFM height images of PM6:PY-IT based organic solar cells in (a-d) thin and (e-h) thick films.

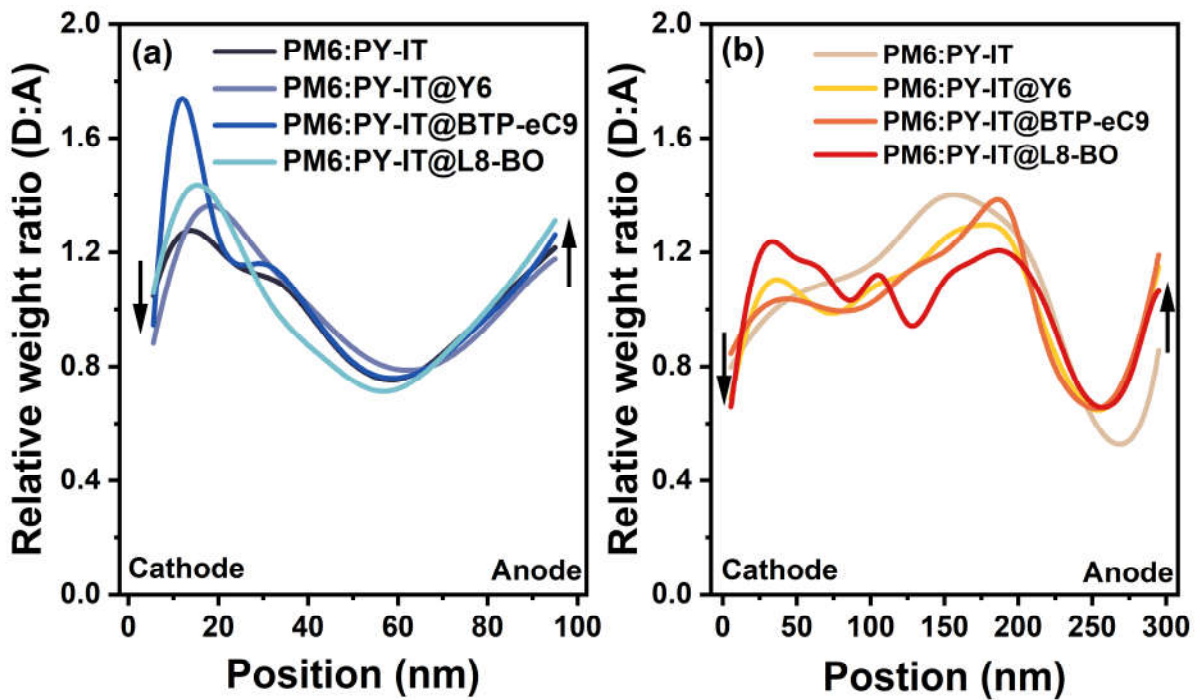


Figure S16. Evolution of vertical phase distribution of PM6:PY-IT-based (a) thin films and (b) thick films.

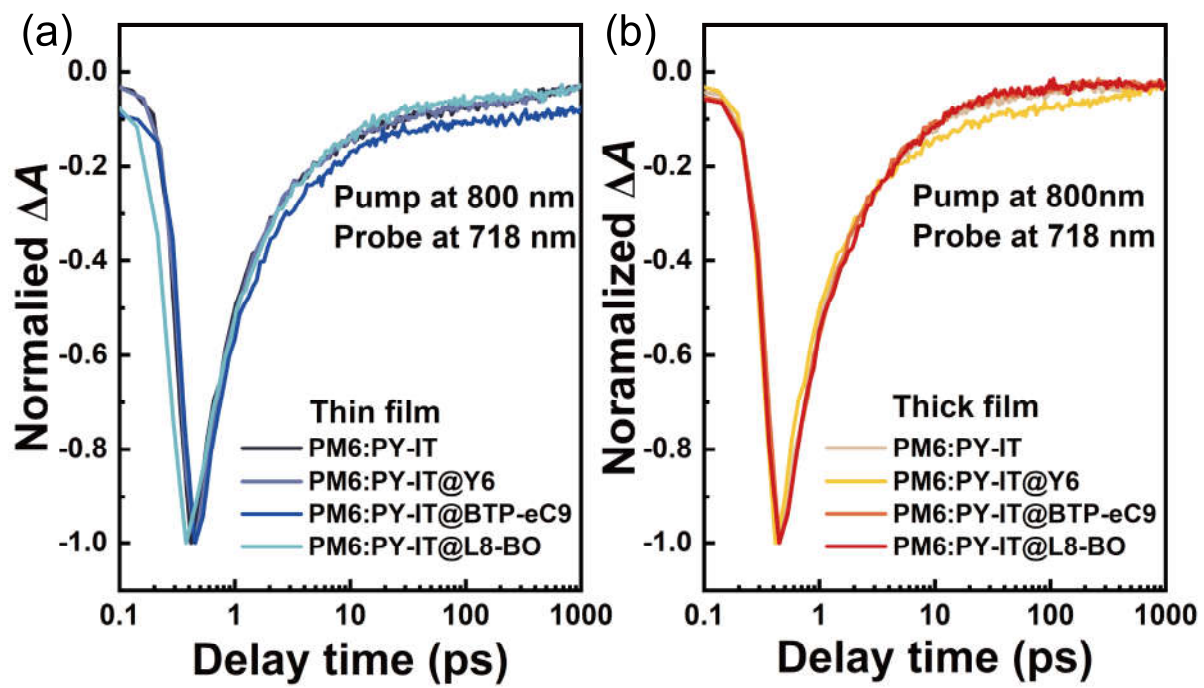


Figure S17. Normalized TAS dynamic curves probed at 718 nm for PM6:PY-IT based (a) thin films and (b) thick films.

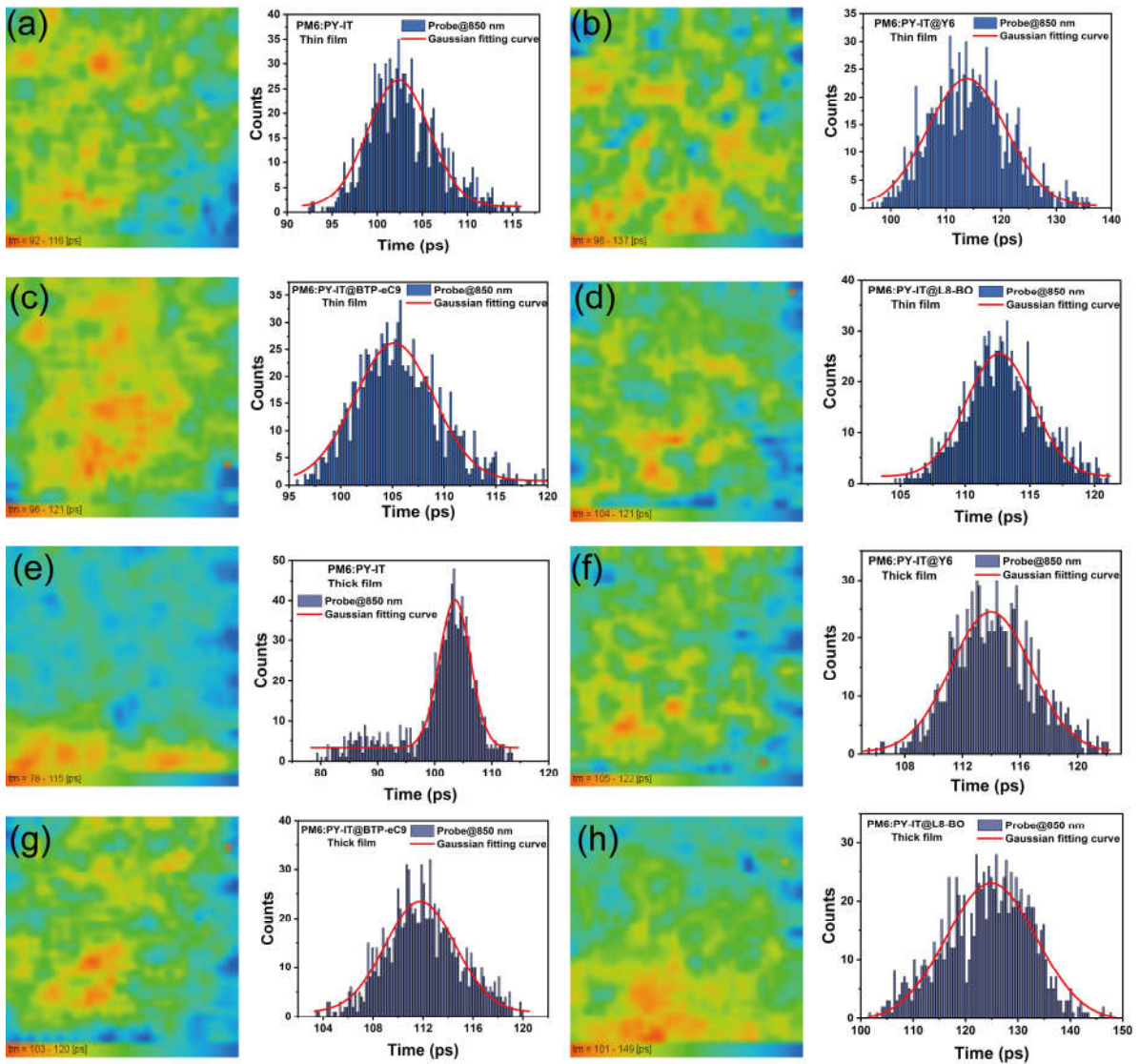


Figure S18. 2D time-resolved photoluminescence images (area: $10 \times 10 \mu\text{m}$) and corresponding distribution histogram of fluorescence lifetime probed at 850 nm of PM6:PY-IT based (a-d) thin and (e-h) thick films.

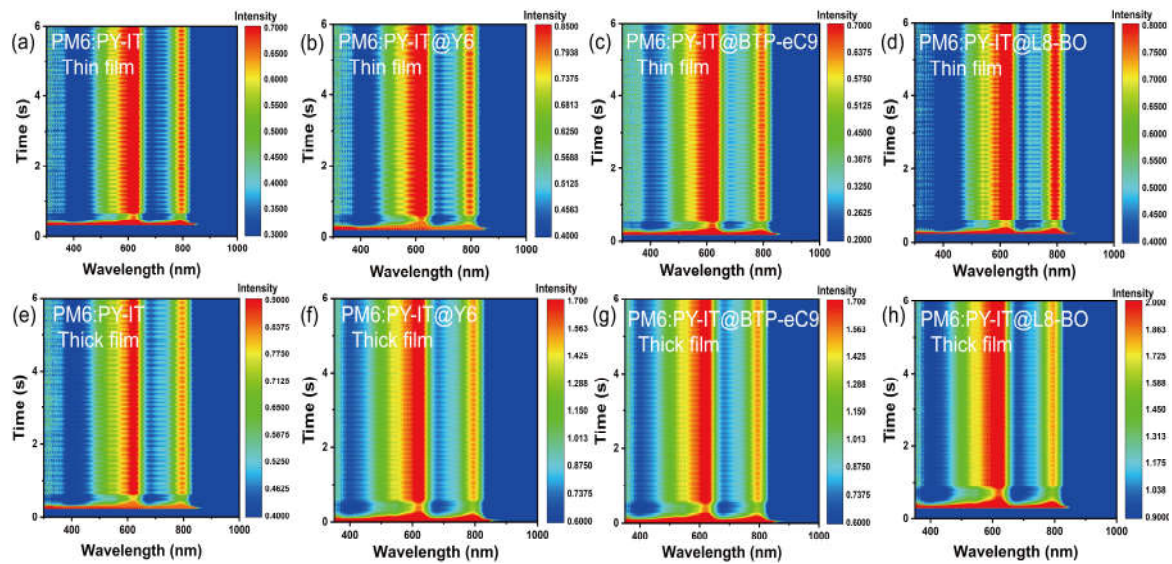


Figure S19. In situ 2D UV-vis absorption of PM6:PY-IT based (a-d) thin and (e-h) thick films.

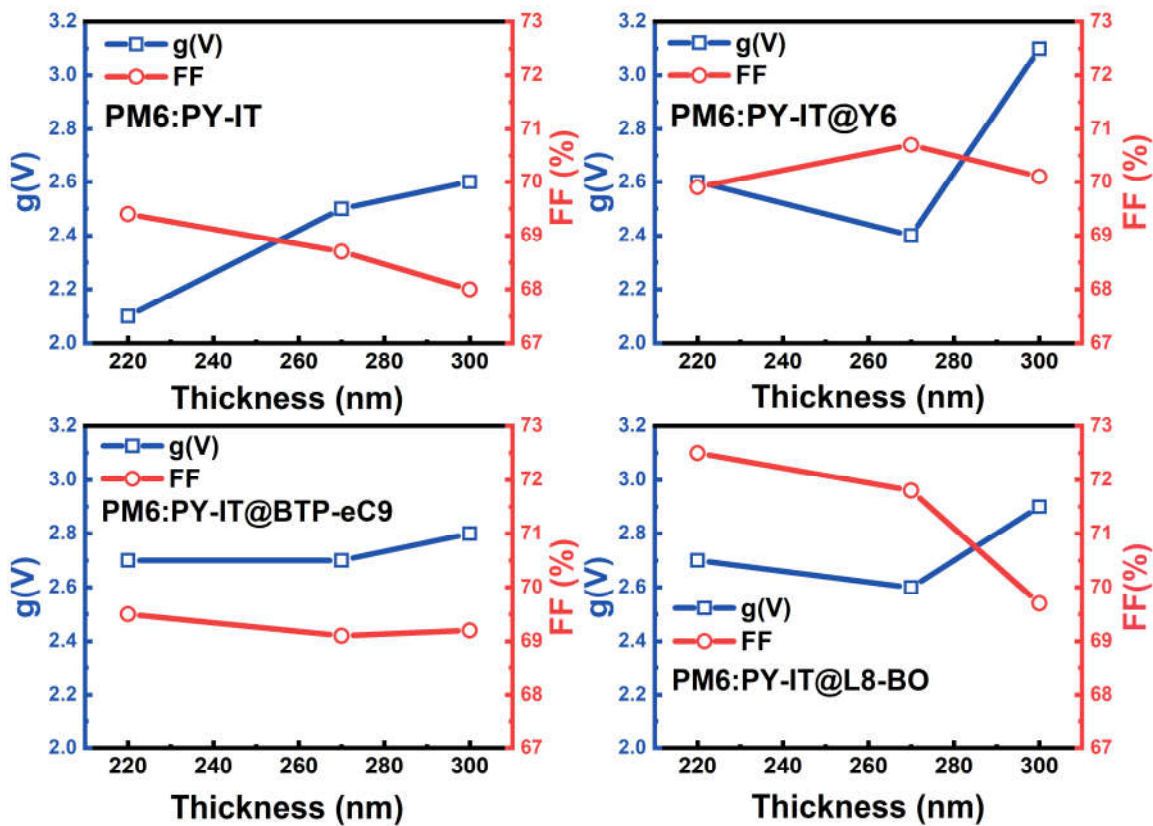


Figure S20. Electron transport characteristic $g(V)$ versus FF in PM6:PY-IT-based APSCs with different active layer thicknesses.

Table S1. Mobilities estimated from SCLC measurements.

Pristine films	μ ($\text{cm}^2\text{V}^{-1}\text{s}^{-1}$)
Y6	2.3×10^{-5}
BTP-eC9	2.6×10^{-4}
L8-BO	1.1×10^{-5}
PY-IT	5.6×10^{-4}
PC ₇₁ BM	6.7×10^{-4}
Y7	3.8×10^{-4}
N3	4.7×10^{-4}
IT-4F	8.0×10^{-5}
ITIC	7.3×10^{-6}
IEICO	9.2×10^{-6}
IEICO-4F	2.2×10^{-5}
PYF-T- <i>o</i>	6.5×10^{-4}
N2200	1.7×10^{-5}
PM6	6.0×10^{-5}
PBDB-T	1.4×10^{-5}
PTB7-Th	1.4×10^{-4}

Table S2. Mobilities obtained from SCLC measurements.

Blends	Thickness (nm)	μ_e ($\text{cm}^2\text{V}^{-1}\text{s}^{-1}$)	Thickness (nm)	μ_h ($\text{cm}^2\text{V}^{-1}\text{s}^{-1}$)
PM6:Y7	200	1.1×10^{-4}	220	5.3×10^{-6}
PM6:N3	160	4.6×10^{-5}	190	1.0×10^{-6}
PM6:IT-4F	400	1.9×10^{-4}	420	4.2×10^{-5}
PBDB-T:ITIC	200	4.8×10^{-4}	200	2.5×10^{-5}
PTB7-Th:IEICO	200	3.2×10^{-5}	150	3.9×10^{-5}

Table S3. Mobilities obtained from SCLC measurements.

Blends	Thickness (nm)	μ_e ($\text{cm}^2\text{V}^{-1}\text{s}^{-1}$)	Thickness (nm)	μ_h ($\text{cm}^2\text{V}^{-1}\text{s}^{-1}$)
PTB7-Th:IEICO-4F	200	1.7×10^{-5}	150	5.2×10^{-5}
PM6:PYF-T- <i>o</i>	200	2.2×10^{-5}	350	2.8×10^{-5}
PBDB-T:N2200	200	8.1×10^{-4}	220	1.7×10^{-5}
PM6- <i>b</i> -PTY6	180	2.4×10^{-6}	220	1.6×10^{-6}
PBDB-T- <i>b</i> -PTY6	150	1.9×10^{-5}	180	3.1×10^{-5}

Table S4. Mobilities obtained from admittance spectroscopy (AS), dark-injection (DI) SCLC and SCLC measurements for PM6:Y6 film.

Measurements	μ_e ($\text{cm}^2\text{V}^{-1}\text{s}^{-1}$)	β_e (cm/V) $^{1/2}$	μ_h ($\text{cm}^2\text{V}^{-1}\text{s}^{-1}$)	β_h (cm/V) $^{1/2}$
AS	5.5×10^{-5}	9.6×10^{-4}	1.6×10^{-5}	1.8×10^{-3}
DI-SCLC	2.6×10^{-4}	1.1×10^{-4}	1.3×10^{-5}	3.8×10^{-4}
SCLC	4.1×10^{-5}	0	5.6×10^{-5}	9.8×10^{-4}

Table S5. Summary of Urbach energy (E_U) values obtained from photothermal deflection spectroscopy (PDS) and sensitive sub-bandgap external quantum efficiency (s-EQE) for five typical BHJs.

Blends	E_U (PDS)	E_U (s-EQE)
	meV	meV
PM6:Y6	25.4	24.6
PM6:BTP-eC9	25.5	24.9
PM6:L8-BO	23.8	23.0
PM6:PY-IT	24.3	23.4
PM6:PC ₇₁ BM	55.7	52.4

Table S6. Photovoltaic parameters of the APSCs based on PM6:PY-IT with different solid additive, under illumination of AM 1.5G, 100 mW cm⁻².

Solid additive (2 wt%)	Thickness (nm)	V _{oc} (V)	J _{SC} (mA/cm ²)	J _{SC,cal.^a} (mA/cm ²)	FF (%)	PCE ^b (%)
None	100	0.947	24.19	23.56	76.7	17.56 (17.19 ± 0.23)
	120	0.943	24.29	23.73	76.2	17.45 (17.23 ± 0.17)
	150	0.941	24.04	23.40	75.5	17.08 (16.70 ± 0.22)
	270	0.932	25.11	24.26	68.7	16.08 (15.88 ± 0.13)
	300	0.927	24.98	24.27	68.0	15.75 (15.54 ± 0.17)
Y6	100	0.946	25.11	24.19	75.5	17.93 (17.67 ± 0.20)
	120	0.943	24.85	24.16	75.6	17.72 (17.43 ± 0.22)
	150	0.934	24.77	23.91	75.2	17.40 (17.20 ± 0.12)
	270	0.926	25.29	24.35	70.7	16.56 (16.36 ± 0.15)
	300	0.929	25.51	24.40	70.1	16.61 (16.30 ± 0.12)
BTP-eC9	100	0.939	24.97	24.11	75.5	17.70 (17.35 ± 0.24)
	120	0.934	25.22	24.43	75.9	17.88 (17.72 ± 0.13)
	150	0.935	24.74	23.99	75.0	17.35 (17.17 ± 0.13)
	270	0.931	25.06	24.23	69.1	16.12 (15.95 ± 0.11)
	300	0.928	24.98	24.27	69.2	16.04 (15.78 ± 0.16)
L8-BO	100	0.945	24.92	24.04	75.6	17.80 (17.42 ± 0.25)
	120	0.942	25.00	24.24	75.4	17.76 (17.56 ± 0.15)
	150	0.938	24.89	24.03	75.5	17.63 (17.42 ± 0.19)
	270	0.932	25.32	24.37	71.8	16.94 (16.75 ± 0.14)
	300	0.930	25.25	24.32	69.7	16.37 (16.20 ± 0.10)

The errors are defined as standard deviation.

^a) Denotes integrated J_{SC} from the EQE curves.

^b) average PCE from ten independent cells.

Table S7. The hole mobilities of PM6:PY-IT based thin and thick films.

Solid additive	Thickness (nm)	μ_h ($\text{cm}^2\text{V}^{-1}\text{s}^{-1}$)
None	220	2.9×10^{-5}
	270	5.3×10^{-5}
	300	6.5×10^{-5}
Y6	220	4.1×10^{-5}
	270	7.3×10^{-5}
	300	8.7×10^{-5}
BTP-eC9	220	4.4×10^{-5}
	270	6.3×10^{-5}
	300	6.7×10^{-5}
L8-BO	220	6.2×10^{-5}
	270	9.7×10^{-5}
	300	1.1×10^{-4}

Table S8. Detailed lifetimes of dissociation and diffusion processes of PM6:PY-IT based thin and thick films.

Solid additive	Thickness (nm)	τ_1 (ps)	A_1 (%)	τ_2 (ps)	A_2 (%)
None	100	0.45	84.49	4.62	15.51
	300	0.49	81.48	4.82	18.52
Y6	100	0.45	85.50	4.62	14.50
	300	0.45	84.41	4.66	15.59
BTP-eC9	100	0.47	83.15	4.80	16.85
	300	0.53	80.66	4.63	19.34
L8-BO	100	0.52	80.50	5.14	19.50
	300	0.52	79.01	4.82	20.99

Table S9. The mean exciton lifetime of PM6:PY-IT based thin and thick films.

Solid additive	Thickness (nm)	τ (ps)
None	100	102.4
	300	103.5
Y6	100	113.8
	300	114.0
BTP-eC9	100	105.2
	300	111.8
L8-BO	100	112.7
	300	124.9

Table S10. The electron mobilities of PM6:PY-IT based thin and thick films.

Solid additive	Thickness (nm)	μ_e ($\text{cm}^2\text{V}^{-1}\text{s}^{-1}$)
None	220	3.7×10^{-4}
	270	1.6×10^{-4}
	300	2.3×10^{-4}
Y6	220	9.5×10^{-5}
	270	1.2×10^{-4}
	300	2.7×10^{-4}
BTP-eC9	220	2.4×10^{-4}
	270	5.0×10^{-4}
	300	2.6×10^{-4}
L8-BO	220	9.2×10^{-5}
	270	1.2×10^{-4}
	300	2.3×10^{-4}

Table S11. Photovoltaic performance parameters of the high-efficiency APSCs with thick photoactive layer reported in the literatures.

Devices	Thickness (nm)	PCE (%)	Reference
PM6:PY-82:PY-DT	120	18.03	[7]
	200	16.08	
	300	15.70	
PM6:PYTT	89	12.35	[8]
	103	12.69	
	112	13.58	
	127	13.52	
	140	13.31	
	192	13.44	
JD40:PJTWT	120	16.31	[9]
	210	14.72	
	250	14.00	
	300	13.43	
JD40:PJTET	120	10.93	[9]
	175	8.22	
	185	7.46	
PBDB-T:PFY-3Se	110	15.1	[10]
	185	13.5	
	210	12.9	
	250	12.4	
PM6:PTQ10:PY-IT	138	16.52	[11]
	205	15.27	
	306	13.91	
PM6:PBB2-H:PY-IT	100	17.64	[12]
	300	16.56	

References

- [1] X. G. Zhang, S. T. Pantelides, Phys. Rev. Lett. 108 (2012) 266602.
- [2] H. FrÖHlich, Nature 164 (1949) 377-377.
- [3] A. Rose, Phys. Rev 97 (1955) 1538-1544.
- [4] M. A. Lampert, Phys. Rev 103 (1956) 1648-1656.
- [5] P. Mark, W. Helfrich, J. Appl. Phys. 33 (2004) 205-215.
- [6] J. Frenkel, Phys. Rev 54 (1938) 647-648.
- [7] Y. Cai, C. Xie, Q. Li, C. Liu, J. Gao, M. H. Jee, J. Qiao, Y. Li, J. Song, X. Hao, H. Y. Woo, Z. Tang, Y. Zhou, C. Zhang, H. Huang, Y. Sun, Adv. Mater. 35 (2023) 2208165.
- [8] J. Ji, L. Zhu, X. Xiong, F. Liu, Z. Liang, Adv. Sci. 9 (2022) 2200864.
- [9] J. Zhang, C.-H. Tan, K. Zhang, T. Jia, Y. Cui, W. Deng, X. Liao, H. Wu, Q. Xu, F. Huang, Y. Cao, Adv. Energy. Mater. 11 (2021) 2102559.
- [10] Q. Fan, H. Fu, Q. Wu, Z. Wu, F. Lin, Z. Zhu, J. Min, H. Y. Woo, A. K.-Y. Jen, Angew. Chem. Int. Ed. 60 (2021) 15935-15943.
- [11] W. Zhang, C. Sun, I. Angunawela, L. Meng, S. Qin, L. Zhou, S. Li, H. Zhuo, G. Yang, Z.-G. Zhang, H. Ade, Y. Li, Adv. Mater. 34 (2022) 2108749.
- [12] J. Wang, C. Han, S. Wen, F. Bi, Z. Hu, Y. Li, C. Yang, X. Bao, J. Chu, Energy Environ. Sci. 16 (2023) 2327-2337.